

Modeling of Arrhythmogenic Right Ventricular Cardiomyopathy With Human Induced Pluripotent Stem Cells

Oren Caspi, Irit Huber, Amira Gepstein, Gil Arbel, Leonid Maizels, Monther Boulos and Lior Gepstein

Circ Cardiovasc Genet. 2013;6:557-568; originally published online November 7, 2013;
doi: 10.1161/CIRCGENETICS.113.000188

Circulation: Cardiovascular Genetics is published by the American Heart Association, 7272 Greenville Avenue, Dallas, TX 75231

Copyright © 2013 American Heart Association, Inc. All rights reserved.
Print ISSN: 1942-325X. Online ISSN: 1942-3268

The online version of this article, along with updated information and services, is located on the World Wide Web at:

<http://circgenetics.ahajournals.org/content/6/6/557>

Data Supplement (unedited) at:

<http://circgenetics.ahajournals.org/content/suppl/2013/11/07/CIRCGENETICS.113.000188.DC1.html>

Permissions: Requests for permissions to reproduce figures, tables, or portions of articles originally published in *Circulation: Cardiovascular Genetics* can be obtained via RightsLink, a service of the Copyright Clearance Center, not the Editorial Office. Once the online version of the published article for which permission is being requested is located, click Request Permissions in the middle column of the Web page under Services. Further information about this process is available in the [Permissions and Rights Question and Answer](#) document.

Reprints: Information about reprints can be found online at:
<http://www.lww.com/reprints>

Subscriptions: Information about subscribing to *Circulation: Cardiovascular Genetics* is online at:
<http://circgenetics.ahajournals.org/subscriptions/>

Modeling of Arrhythmogenic Right Ventricular Cardiomyopathy With Human Induced Pluripotent Stem Cells

Oren Caspi, MD, PhD; Irit Huber, PhD; Amira Gepstein, PhD; Gil Arbel, MSc; Leonid Maizels, MSc; Monther Boulos, MD; Lior Gepstein, MD, PhD

Background—Arrhythmogenic right ventricular cardiomyopathy (ARVC) is a primary heart muscle disorder resulting from desmosomal protein mutations. ARVC is characterized pathologically by fibrofatty infiltration and clinically by arrhythmias and sudden cardiac death. We aimed to establish a patient-/disease-specific human induced pluripotent stem cell (hiPSC) model of ARVC.

Methods and Results—Dermal fibroblasts were obtained from 2 patients with ARVC with plakophilin-2 (*PKP2*) mutations, reprogrammed to generate hiPSCs, coaxed to differentiate into cardiomyocytes (CMs), and then compared with healthy control hiPSC-derived CMs (hiPSC-CMs). Real-time polymerase chain reaction showed a significant decrease in the expression of *PKP2* in the ARVC-hiPSC-CMs. Immunostainings revealed reduced densities of *PKP2*, the associated desmosomal protein plakoglobin, and the gap-junction protein connexin-43. Electrophysiological assessment demonstrated prolonged field potential rise time in the ARVC-hiPSC-CMs. Transmission electron microscopy identified widened and distorted desmosomes in the ARVC-hiPSC-CMs. Clusters of lipid droplets were identified in the ARVC-CMs that displayed the more severe desmosomal pathology. This finding was associated with upregulation of the proadipogenic transcription factor peroxisome proliferator-activated receptor- γ . Exposure of the cells to adipogenic stimuli augmented desmosomal distortion and lipid accumulation. The latter phenomenon was prevented by application of a specific inhibitor of glycogen synthase kinase 3 β (6-bromoindirubin-3'-oxime).

Conclusions—This study highlights the unique potential of the hiPSC technology for modeling inherited cardiac disorders in general and ARVC specifically. The hiPSC-CMs were demonstrated to recapitulate the ARVC phenotype in the dish, provide mechanistic insights into early disease pathogenesis, and provide a unique platform for drug discovery and testing in this disorder. (*Circ Cardiovasc Genet.* 2013;6:557-568.)

Key Words: arrhythmogenic right ventricular dysplasia ■ lipids ■ myocytes, cardiac ■ stem cells

Arrhythmogenic right ventricular cardiomyopathy (ARVC) is a heritable primary cardiac muscle disorder characterized by the replacement of cardiomyocytes (CMs), primarily in the right ventricle (RV), by fibrofatty tissue.^{1,2} The resulting disruption of normal myocardial architecture can lead to RV dysfunction, life-threatening arrhythmias, and sudden cardiac death. Causative mutations have been identified in a significant number of patients, mainly in genes encoding for proteins associated with mechanical cell junctions (plakoglobin, plakophilin, desmoglein, desmocollin, and desmoplakin).^{3,4} Mutated gene products were shown to be involved in remodeling of the intercalated disc.

Clinical Perspective on p 568

Significant insights into ARVC pathogenesis have been gained in the past decade from several clinical, genetic, and pathological studies in patients with ARVC⁵ and from relevant

mouse models.⁶ Nevertheless, among the hurdles in studying the disease process has been the inability to study viable human CMs from patients with ARVC. The introduction of the induced pluripotent stem cell (iPSC) technology⁷ may provide a possible solution to this challenge. The human iPSC (hiPSC) approach allows reprogramming of adult somatic cells into pluripotent stem cells by expression of a set of transcription factors.⁸ Recent studies demonstrated the robust ability to generate hiPSCs and to coax their differentiation into the cardiac lineage.^{9,10} More recent studies showed the ability to establish disease-/patient-specific hiPSCs that can model disease-specific abnormalities in several inherited cardiac disorders such as different variants of the long-QT syndrome,^{11,12} dilated and hypertrophic cardiomyopathies,^{13,14} and catecholaminergic polymorphic ventricular tachycardia.¹⁵

In the current study, we aimed to use the emerging hiPSC technology to establish an in vitro model of ARVC. We

Received February 5, 2013; accepted October 19, 2013.

From the Sohni Family Research Laboratory for Cardiac Electrophysiology and Regenerative Medicine, Rappaport Faculty of Medicine and Research Institute, Technion-Israel Institute of Technology, Haifa, Israel (O.C., I.H., A.G., G.A., L.M., L.G.); and Department of Internal Medicine B (O.C.) and Cardiology (M.B., L.G.), Rambam Medical Center, Haifa, Israel.

The online-only Data Supplement is available at <http://circgenetics.ahajournals.org/lookup/suppl/doi:10.1161/CIRCGENETICS.113.000188/-DC1>.

Correspondence to Lior Gepstein, MD, PhD, Technion's Faculty of Medicine, POB 9649, Haifa 31096, Israel. E-mail mdlior@tx.technion.ac.il

© 2013 American Heart Association, Inc.

Circ Cardiovasc Genet is available at <http://circgenetics.ahajournals.org>

DOI: 10.1161/CIRCGENETICS.113.000188

hypothesized that CMs differentiating from the ARVC-hiPSCs will recapitulate the disease phenotype and that investigation of these cells may provide new insights into the disease process.

Materials and Methods

An expanded description of the methods used for genomic sequencing, teratoma formation, karyotype analysis, immunostainings, terminal deoxynucleotidyl transferase dUTP nick end labeling staining, gene expression analysis, microelectrode array recordings, and transmission electron microscopy is provided in the online-only Data Supplement.

Establishment and CM Differentiation of the ARVC-hiPSCs

All studies were approved by the Helsinki committee of Rambam Medical Center, Haifa, Israel. Dermal fibroblasts were isolated from a small skin biopsy obtained after the patients' informed consent. The hiPSCs were established by retroviral delivery of *Oct4*, *Sox2*, and *Klf4* followed by valproic acid treatment as described.^{11,16} Several ARVC-hiPSC clones, which were positively stained with vital Tra-I-60 staining, were selected and expanded. Undifferentiated hiPSC colonies were cultured on mouse embryonic fibroblasts as previously described.^{11,16} Culture medium consisted of 80% knock-out high-glucose glutamine-free DMEM with sodium pyruvate supplemented with 20% serum replacement, L-glutamine 1 mmol/L, mercaptoethanol 0.1 mmol/L, bFGF 4 ng/mL, and 1% nonessential amino acids (Invitrogen).

CM differentiation of the ARVC and healthy control hiPSCs was induced using the embryoid body (EB) differentiating system.¹⁷ Briefly, undifferentiated hiPSCs were dispersed into small cell clumps using collagenase IV (300 U/mL for 45 minutes; Life Technologies) and cultivated in suspension for 10 days as EBs. The EBs were plated on 0.1% gelatin-coated culture dishes. Spontaneously contracting area was microdissected and used for phenotypic characterization.

Adipogenic Medium

In some of the studies, the hiPSC-derived CMs (hiPSC-CMs) were cultured in an adipogenic-promoting medium. Adipogenesis was promoted in a similar manner to that reported previously¹⁸⁻²¹ with slight modifications. Briefly, microdissected control and ARVC-hiPSC-CMs (at 30 days of differentiation) were treated with 20% fetal bovine serum-containing media supplemented with 10 μ g/mL insulin (Biological Industries, Israel), 0.5 mmol/L 3-isobutyl-1-methylxanthine (Sigma-Aldrich), 2.5 μ mol/L dexamethasone (Sigma-Aldrich), and StemPro LipoMax²⁰ (1:200) for 3 days. Fresh media containing 20% FBS supplemented with insulin (10 μ g/mL) and StemPro-LipoMax (1:200) was then replaced every other day for an additional 14 days. In the experiments evaluating GSK-3 β inhibition, 10 μ mol/L of 6-bromoindirubin-3'-oxime (BIO; Sigma-Aldrich) was added.

Statistical Analysis

Continuous variables are reported as mean \pm SEM. Categorical variables are expressed as frequencies. Differences between group means were compared using the Mann-Whitney *U* test (except for differences between drug treatment and baseline in which the Wilcoxon test was used). Comparison between lipid accumulation and desmosomal gap width quartiles was conducted using the χ^2 for trend analysis. Receiver operating characteristic curve analysis was used to assess the sensitivity and specificity of desmosomal gap width as a marker and a predictor of lipid droplet accumulation. To this aim, desmosomal gap width was used as a continuous variable (width measured in nm), and lipid droplet accumulation within the same cell was used as a categorical binary value. Receiver operating characteristic curve analysis was conducted using SPSS-16. We calculated the area under the curve, also known as concordance statistic, to assess discrimination. A value of *P*<0.05 was considered statistically significant.

Results

Generation of the ARVC Patient-Specific hiPSCs

Dermal fibroblasts were obtained from a 30-year-old man diagnosed previously with ARVC according to the 2010 task force criteria for ARVC.²² Clinically, the patient presented with episodes of rapid palpitations, near-syncope, and a family history of sudden cardiac death. His baseline ECG revealed typical T-wave inversions in leads V1 through V3 (Figure 1A). Episodes of ventricular tachycardia were also recorded, displaying a left bundle branch block-like morphology (Figure 1B). Echocardiographic examination and RV ventriculography revealed a dilated and trabeculated RV with reduced global RV function and segmental wall motion abnormalities. Electroanatomic mapping of the RV identified large areas with reduced voltage (Figure 1C), a finding previously shown to correlate with the diseased RV regions.²³

Genetic analysis identified a heterozygous insertion of T in position 972 in exon 3 of the plakophilin-2 (*PKP2*) gene (c.972InsT/N), resulting in a frame shift from amino acid 324 to a stop codon in position 335 (A324fs335X). This mutation has not been previously reported. The patient's fibroblasts were reprogrammed to generate the patient-specific ARVC-hiPSCs by retroviral delivery of *Oct3/4*, *Sox2*, and *Klf4*. Similar hiPSCs previously created from fibroblasts of a healthy individual using an identical reprogramming strategy served as controls.¹⁶ Sequencing of the affected allele (Figure 1D) verified that the *PKP2* mutation was present in the ARVC-hiPSC colonies but not in healthy control cells.

The ARVC-hiPSC colonies displayed typical human embryonic stem cell morphology (Figure 2A, left), were stained positively for the pluripotent markers Oct-4, NANOG, SSEA-4, and Tra-I-60 (Figure 2A), displayed alkaline phosphatase activity (Figure 2B), and maintained a normal karyotype. Pluripotency of the ARVC-hiPSCs was verified by the presence of cell derivatives of all 3 germ layers in in vitro differentiating EBs, as manifested by the positive staining for Desmin (mesoderm), α -fetoprotein (endoderm), and nestin (ectoderm; Figure 2C). Similarly, injection of undifferentiated ARVC-hiPSCs into SCID-beige mice led to the formation of teratomas containing advanced tissue derivatives of all 3 germ layers (Figure 2D). Finally, ARVC-hiPSCs showed silencing of the 3 retroviral transgenes (Figure 2E) and reactivation of endogenous pluripotency genes (*NANOG*, *FOXD3*, and *OCT4*; Figure 2F), indicating successful reprogramming.

CM Differentiation

The EB differentiation system was used to coax the differentiation of the hiPSCs into the cardiac lineage (Movie I in the online-only Data Supplement). Real-time quantitative polymerase chain reaction (PCR) analysis showed comparable levels of expression of cardiac-specific genes in the ARVC and healthy control hiPSC-CMs and minimal expression of these genes in the undifferentiated cells (Figure 3A). Similarly, immunostainings of the sarcomeric proteins cardiac troponin I and α -actinin (Figure 3B) confirmed the CM phenotype of the differentiating hiPSC-CMs.

Extracellular multielectrode array recordings established the presence of cardiac-specific electric activity by the ARVC-hiPSC-CMs (Figure 3C) and the development of a functional syncytium with pacemaker activity and action

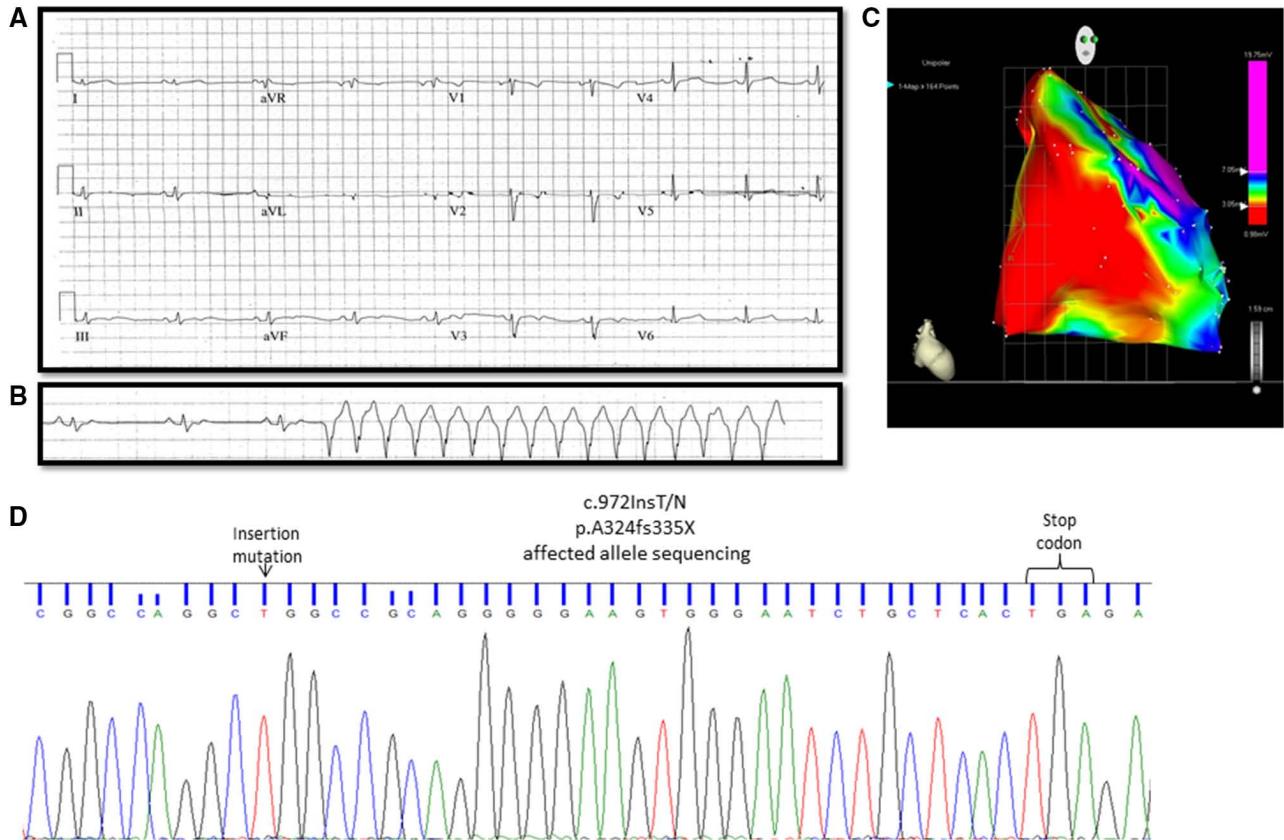


Figure 1. Clinical characteristics of the patient with arrhythmogenic right ventricular cardiomyopathy (ARVC). **A**, Twelve-lead ECG of the patient with ARVC showing inverted T waves in leads V1 through V3. **B**, Electrocardiographic tracing showing the development of ventricular tachycardia in the patient with ARVC. **C**, Right anterior oblique view of the electroanatomic unipolar voltage map of the right ventricle (RV) of the patient with ARVC. Note the extensive area of low voltage (red indicates unipolar electrograms <3 mV), corresponding to the diseased regions in the RV inflow, outflow, and anterolateral free wall. **D**, Sequencing of the mutated allele of the plakophilin-2 (*PKP2*) gene in the ARVC-hiPSCs confirming the insertion of T in position 972 in exon 3 of the *PKP2* gene (c.972InsT), which results in a stop codon in position 335 (A324fs335X/N). hiPSC indicates human induced pluripotent stem cell.

potential propagation (Figure 3D; Movie II in the online-only Data Supplement). Adequate chronotropic responses to adrenergic and cholinergic stimuli were noted after application of 10 $\mu\text{mol/L}$ isoproterenol (increase in beating frequency by $156 \pm 55\%$; $P < 0.05$; $n = 5$) and 1 $\mu\text{mol/L}$ carbamylcholine (decrease in beating frequency by $45 \pm 12\%$; $P < 0.05$; $n = 5$).

Automated analysis of the field potential rise time, previously suggested as a surrogate marker for the cellular action potential rise time,²⁴ revealed significant prolongation of this parameter in the ARVC-hiPSC-CMs compared with healthy control cells (11.5 ± 2.6 versus 4.1 ± 1.3 ms, respectively; $P < 0.05$; Figure 3E). Finally, analysis of the corrected field potential duration revealed a slightly prolonged corrected field potential duration in ARVC-hiPSC-CMs, which was not statistically significant compared with healthy control cells (0.36 ± 0.02 seconds versus 0.42 ± 0.03 seconds).

Immunostaining for Desmosomal and Gap-Junction Proteins

Because the mutations associated with ARVC involve mainly desmosomal proteins, we initially performed real-time quantitative PCR analysis evaluating the expression of the relevant genes in ARVC and healthy control hiPSC-CMs. These studies revealed a significant reduction in the expression of *PKP2* in the ARVC-CMs compared with healthy control cells

($P < 0.01$). In contrast, no significant reductions were noted in the expression of the associated desmosomal genes *JUP* (plakoglobin) and *DSP* (desmoplakin; Figure 4A).

We next performed immunostainings, targeting the desmosomal proteins in small cell clusters of both healthy control and ARVC-hiPSC-CMs (Figure 4B). We initially focused on the evaluation of the staining pattern of *PKP2* (Figure 4B, top). Note the typical membranous punctuate staining pattern for *PKP2* in the healthy control hiPSC-CMs (Figure 4B, top left) and the diminished *PKP2* immunosignal in the ARVC-CMs (Figure 4B, top right). Thus, as expected from the nature of the *PKP2* mutation in the patient with ARVC, quantitative analysis revealed a significant reduction in the density of the *PKP2* immunosignal (expressed as percentage of the total CM cellular area) in the ARVC-hiPSC-CMs compared with healthy control cells ($2.2 \pm 0.6\%$ versus $9.5 \pm 3.6\%$; $P < 0.05$; Figure 4C, top).

In a similar manner, immunostaining analysis for the structurally associated desmosomal protein plakoglobin (also known as γ -catenin) revealed a significant reduction ($P < 0.05$) in the immunofluorescent signal area density in the ARVC ($1.0 \pm 0.1\%$) compared with healthy control ($7.4 \pm 0.9\%$) CMs (Figure 4B and 4C, middle). Finally, we also evaluated the effect of the *PKP2* mutation on the associated intercalated disc structure, gap junction. Interestingly, immunofluorescence analysis, targeting the major

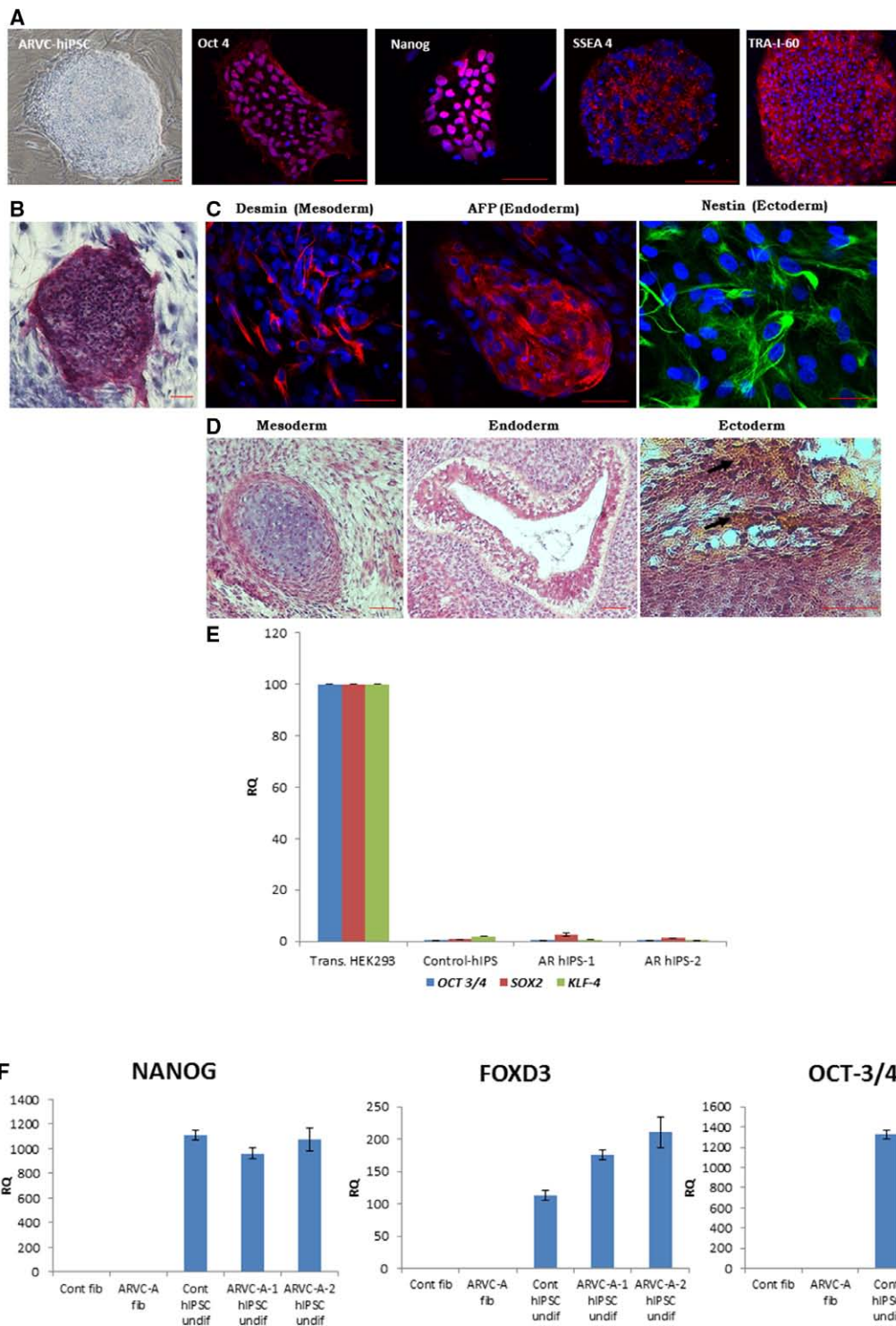


Figure 2. Derivation and characterization of the ARVC-hiPSCs. **A**, Phase contrast (left) and immunofluorescent staining of the ARVC-hiPSC colonies for the pluripotency markers NANOG, OCT4, SSEA4, and TRA-1-60. **B**, Positive staining of the ARVC-hiPSC colonies for alkaline phosphatase. **C**, Immunostaining of in vitro differentiating embryoid bodies for Desmin (mesoderm), α -Fetoprotein (AFP; endoderm), and Nestin (ectoderm). **D**, Teratoma formation in SCID mice after injection of undifferentiated ARVC-hiPSCs. Note the presence of hyaline cartilage (mesoderm), columnar-lining epithelium (endoderm), and melanocytes (ectoderm). Scale bars for **A** to **D**, 50 μ m. **E**, Real-time quantitative PCR showing the downregulation of *OCT3/4*, *KLF4*, and *SOX2* transgenes in the ARVC-hiPSCs (in 2 clones: AR-hiPS-1 and AR-hiPS-2). Values are normalized to the house-keeping gene *RPL-7* and expressed as mean \pm SEM. Expression values (relative quantification [RQ]) are relative to HEK293T cells (HEK) transiently transfected with the 3 plasmids to produce reprogramming virions (n=3 biological repetitions with 3 technical replicates for each biological repetition). **F**, Real-time quantitative PCR evaluating the endogenous levels of the pluripotency genes *NANOG*, *FOXD3*, and *OCT3/4* in healthy control fibroblasts, ARVC fibroblasts, control hiPSCs, and ARVC-hiPSC clones (1 and 2). Values are normalized to the house-keeping gene *RPL-7* and expressed as mean \pm SEM. Expression values (RQ-%) are relative to the levels in the patient's fibroblasts (n=3). ARVC indicates arrhythmogenic right ventricular cardiomyopathy; and hiPSC, human induced pluripotent stem cell.

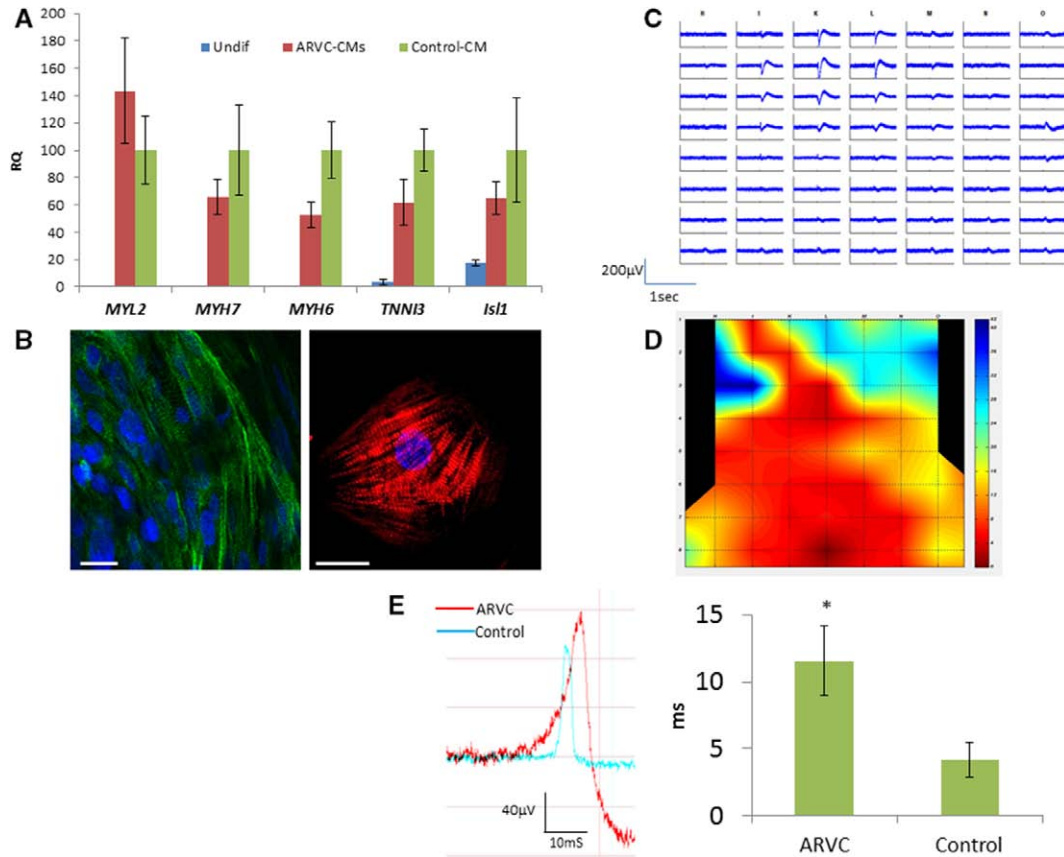


Figure 3. Cardiomyocyte (CM) differentiation. **A**, Real-time PCR analysis showing comparable levels of expression of the cardiac-specific genes *MYL2* (MLC-2v), *MYH7* (β -MHC), *MYH6* (α -MHC), *TNNI3* (cardiac troponin I [cTnI]), and *ISL-1* in CMs differentiating from the arrhythmogenic right ventricular cardiomyopathy (ARVC) and healthy control human induced pluripotent stem cells (hiPSCs). Note also the marked increase in these genes in both CM types compared with the undifferentiated cells ($n=3$). **B**, Immunostaining of differentiating ARVC-hiPSC-CMs for the sarcomeric proteins α -actinin (green; left) and cTnI (red; right). Scale bars, 20 μ m. **C** and **D**, MEA recordings from the ARVC-hiPSC-derived cardiac tissue (**C**). This information is used to generate activation maps (**D**) showing activation propagating from the pacemaker area (red) to the rest of the tissue. **E**, Field potential rise time analysis of extracellular recordings from the ARVC (red) and control (blue) hiPSC-CMs. Note that the ARVC-hiPSC-CMs displayed significant longer rise times ($*P<0.05$, $n=7$). hiPSC-CM indicates hiPSC-derived CM.

gap-junction protein connexin-43 (Cx43), revealed a significant reduction in the Cx43 immunofluorescent signal in the ARVC-hiPSC-CMs compared with healthy control cells ($3.4\pm 0.9\%$ versus $0.9\pm 0.4\%$; $P<0.05$; Figure 4B and 4C, bottom).

Ultrastructural Analysis

To further evaluate the effect of the *PKP2* mutation on the ultrastructural properties of the differentiated ARVC-hiPSC-CMs, we performed transmission electron microscopy analysis of the ARVC and healthy control cells at 40 days of differentiation. Both control and ARVC CMs exhibited large quantities of myofibrils organized into typical sarcomeres by parallel Z bands (Figure 5A and 5B). Interestingly, in 33% (13 of 39) of the ARVC-hiPSC-CMs studied, we could identify the presence of clusters of lipid droplets accumulating within the cytoplasm (Figures 5B, 5E, and 6B). Such a phenomenon was not observed in any of the healthy control hiPSC-CMs.

We next focused on the ultrastructural properties of the desmosomes in the hiPSC-CMs and noted significant morphological differences between healthy control (Figure 5A and 5C) and ARVC (Figure 5B, 5D, and 5E) CMs. This was manifested by the presence of variable degrees of structural distortion of

desmosomes in the ARVC-CMs but not in the healthy control cells. Note the hazy, pale, and dissymmetric appearance of the ARVC desmosomes and the widened desmosomal gaps in the examples provided (Figure 5B, 5D, and 5E). To quantify the degree of desmosomal abnormalities in the ARVC-hiPSC-CMs, we performed quantitative morphometric assessment of the desmosomal dimensions in both the ARVC and control CMs (Figure 5C and 5D). This analysis revealed a significant increase in the desmosomal internal gap width (32 ± 2 versus 24 ± 1 nm; $P<0.05$) and the total external desmosomal width (171 ± 12 versus 101 ± 5 nm; $P<0.01$) in the ARVC-hiPSC-CMs compared with healthy control cells (Figure 5F and 5G).

Strikingly, the degree of desmosomal abnormalities seemed to correlate with the accumulation of lipid droplets within the ARVC-CMs. This can be appreciated in Figures 5B and 6B, in which the presence of severe desmosomal distortion was associated with intracellular accumulation of clusters of lipid droplets. In contrast, ARVC-CMs showing minimal desmosomal abnormalities did not contain similar clusters (Figure 6A).

To further evaluate the relationship between desmosomal abnormalities and accumulation of lipid droplets in the ARVC-hiPSC-CMs, we graded the degree of desmosomal

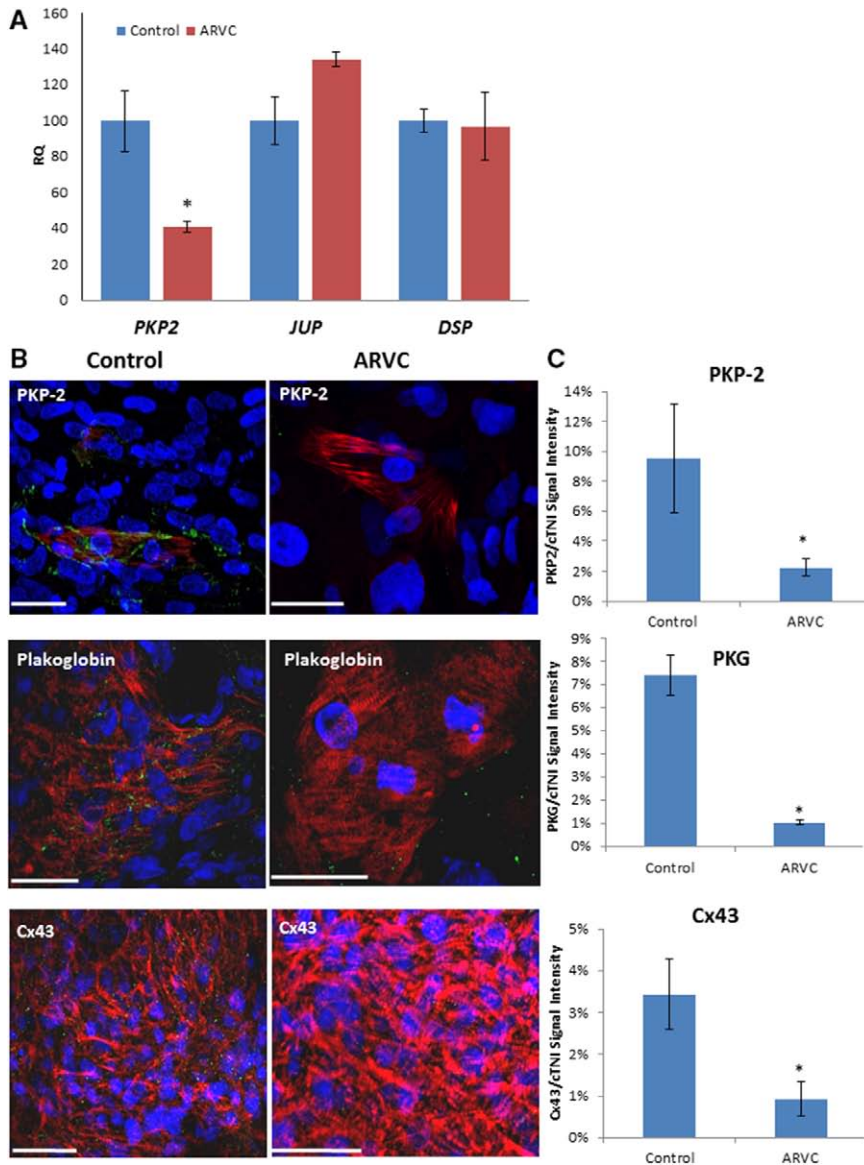


Figure 4. Expression of desmosomal-related proteins. **A**, Real-time PCR analysis quantifying the expression of desmosomal-related genes. Note the significant reduction in the expression of *PKP2* in the ARVC-hiPSC-CMs compared with healthy control cells ($*P<0.05$). No significant differences were noted, however, in the expression levels of *JUP* (plakoglobin) and *DSP* (desmoplakin). Values are normalized to the house-keeping gene *RPL-7* and expressed as mean \pm SEM. Expression values (RQ%) are relative to levels in healthy control CMs. **B** and **C**, Immunostainings of the healthy control (**left**) and ARVC (**right**) hiPSC-CMs targeting *PKP2* (**top**), plakoglobin (**middle**), and Cx43 (**bottom**). **C**, Quantitative evaluation of the density of the *PKP2* ($n=8$; **top**), plakoglobin ($n=9$; **middle**) and Cx43 ($n=8$; **bottom**) immunosignals. Results are described relative to total CM area. Note the significant reduction in the densities of the immunosignals of both desmosomal and gap-junction proteins in the ARVC-hiPSC-CMs (CM clusters; $*P<0.05$). ARVC indicates arrhythmogenic right ventricular cardiomyopathy; hiPSC, human induced pluripotent stem cell; and hiPSC-CM, hiPSC-derived cardiomyocyte.

abnormalities in each cell using the average measured desmosomal gap width within the cell. We then divided all cells into 4 quartiles based on this parameter and compared the percentage of cells containing lipid droplet clusters in each group. As depicted in Figure 6C, lipid accumulation was correlated with desmosomal gap widening quartiles ($P<0.05$). To further assess whether desmosomal abnormalities can predict the presence of lipid accumulation within the cells, we generated a receiver operating characteristic curve. Evaluation of the area under the receiver operating characteristic curve demonstrated a significant correlation between desmosomal gap widening and lipid accumulation (area under the curve=0.84; 95% confidence interval, 0.73–0.94; $n=50$) with an optimal cutoff value of 25.9 nm (Figure 6D).

Finally, we also evaluated, using real-time PCR analysis, the expression level of the master proadipogenic transcription factor peroxisome proliferator-activated receptor- γ . This analysis revealed $>4\times$ increase in the expression levels of peroxisome proliferator-activated receptor- γ in the ARVC-hiPSC-CMs compared with healthy control cells, suggesting

the activation of the adipogenic signaling pathway in these cells (Figure 5H).

Confirmation of the Pathological Findings in a Second ARVC Patient

To evaluate whether the molecular and ultrastructural properties described above may be applicable to other patients with ARVC carrying alternative *PKP2* mutations, we generated a second patient-specific hiPSC line. Dermal fibroblasts were obtained from a 22-year-old patient with ARVC displaying the characteristic RV pathology and ventricular arrhythmias (Figure 1A and 1B in the online-only Data Supplement). Genetic analysis identified a heterozygous deletion of ACAG in positions 148 to 151 in exon 1 of the *PKP2* gene in the defected allele (c.148_151delACAG/N; Figure 1C in the online-only Data Supplement), resulting in replacement of threonine by serine in position 50 and in a frame shift leading to a stop codon in position 110 (p.T50SfsX110). A similar mutation has been previously reported in 4 patients with ARVC.²⁵

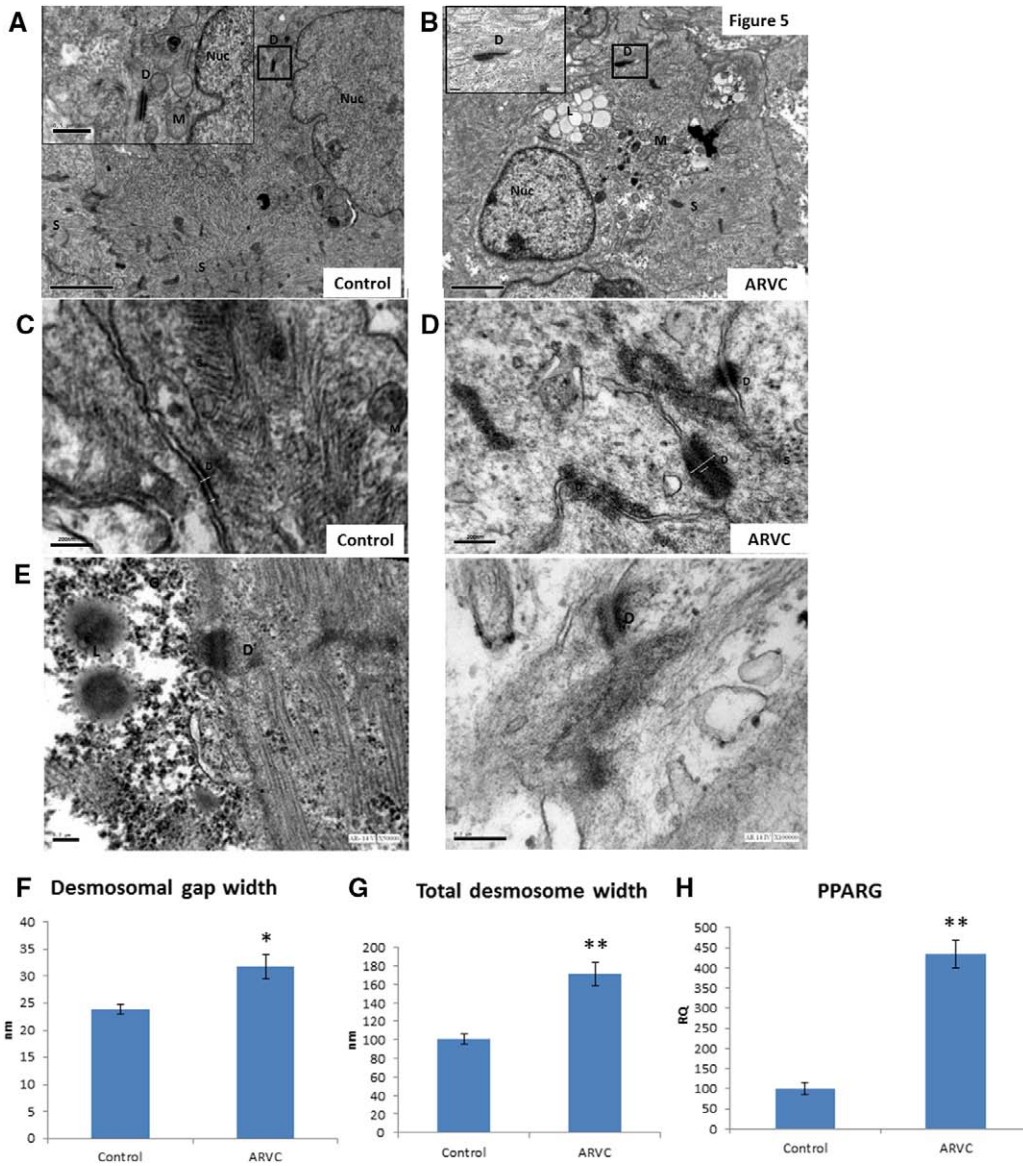


Figure 5. Ultrastructural characterization. **A**, Transmission electron microscopy image of healthy control hiPSC-derived cardiomyocytes (hiPSC-CMs). Note the presence of developing sarcomeres. The intercalated disc area is magnified in the inset and displays a normal looking desmosome. **B**, Transmission electron microscopy image of the ARVC-hiPSC-CMs. Note the presence of a structurally abnormal desmosome in the magnified area (inset). Also note the presence of a cluster of lipid droplets within the ARVC-CM. **C** and **D**, Electron microscopy images showing examples of desmosomes from healthy control (**C**) and ARVC (**D**) hiPSC-CMs. Also shown are the measurements made to analyze desmosomal gap width (short white line) and total desmosome width (long white line). Note the presence of a structurally distorted desmosome in the ARVC-CM with a widened gap and hazy appearance. **E**, Additional high-magnification images depicting distorted desmosomes in ARVC-hiPSC-CMs. **F** and **G**, Quantitative morphometric assessment of the desmosomal gap width (**F**) and total desmosome width (**G**) dimensions. Note the significant increase in these parameters in the ARVC-hiPSC-CMs (* $P < 0.05$, $n = 57$ and ** $P < 0.01$, $n = 57$). **H**, Real-time PCR analysis showing significant upregulation of *PPARG* expression in ARVC-hiPSC-CMs (** $P < 0.01$; $n = 4$). Values are normalized to the house-keeping gene *RPL-7* and expressed as mean \pm SEM. Expression values (RQ%) are relative to levels in healthy control CMs. ARVC indicates arrhythmogenic right ventricular cardiomyopathy; D, desmosome; hiPSC, human induced pluripotent stem cell; L, lipid droplets; M, mitochondria; Nuc, nucleus, and S, sarcomere.

The patient's fibroblasts were reprogrammed to generate ARVC-hiPSCs (ARVC-B) by retroviral delivery of *Oct3/4*, *Sox2*, and *Klf4*. The reprogrammed cells generated typical hiPSC colonies (Figure IIA in the online-only Data Supplement), displayed alkaline phosphatase activity (Figure IIB in the online-only Data Supplement), and stained positively for the same pluripotent markers (Figure IIC in the online-only Data Supplement). Pluripotency of the ARVC-B hiPSCs was verified by the presence of cell derivatives of all

3 germ layers in in vitro differentiating EBs (Figure IID in the online-only Data Supplement). The ARVC-B hiPSCs also showed silencing of the 3 retroviral transgenes (Figure IIE in the online-only Data Supplement) and reactivation of endogenous pluripotency genes (Figure IIF in the online-only Data Supplement), indicating successful reprogramming.

CMs were then derived from the ARVC-B hiPSCs using the same EB-based differentiating technique, and the generated beating areas were also stained positively for cardiac

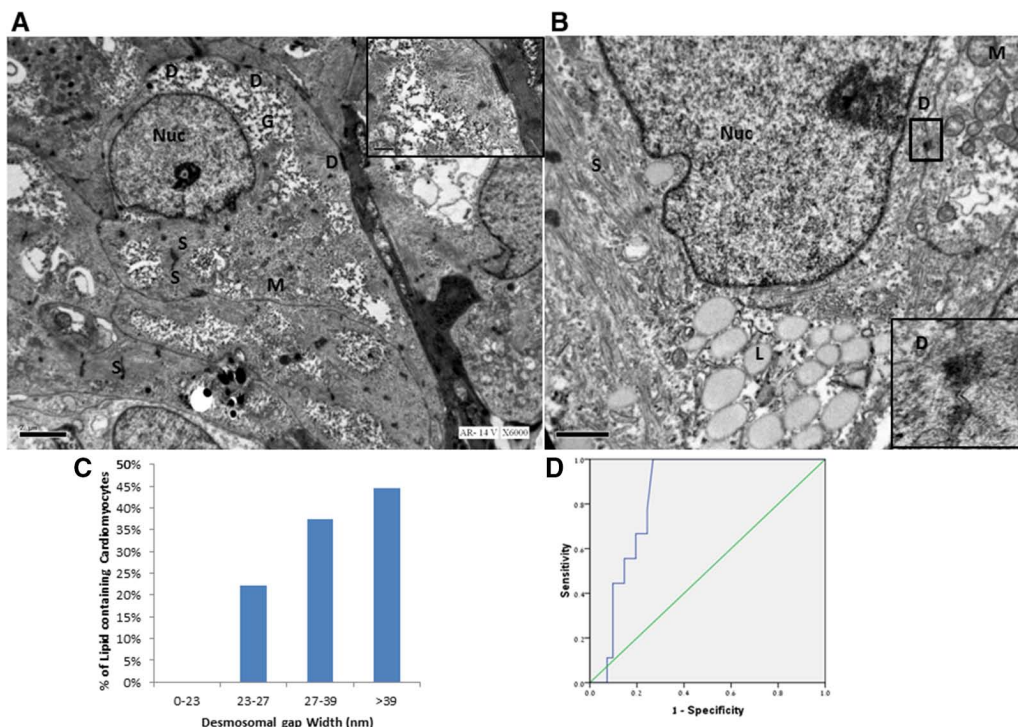


Figure 6. Correlation between desmosomal abnormalities and lipid droplet accumulation. **A** and **B**, Transmission electron microscopy images of a lipid-free (**A**) and a lipid-containing ARVC-hiPSC-CM. Desmosomal distortion, asymmetry, and a widened desmosomal gap (insets) are noted in the lipid-containing cell. In contrast, relatively normal-looking and symmetrical desmosomes are seen in the lipid-free cell. **C**, Frequency of cells showing accumulation of lipid droplet clusters as a function of the desmosomal gap widths (divided to quartiles). Note that cells in the higher quartiles of desmosomal gap widths are associated with a significantly higher probability of containing lipid droplets ($*P<0.05$, χ^2 for trend analysis.). **D**, Receiver operating curve (ROC) depicting the sensitivity and specificity of desmosomal gap width in predicting lipid droplet accumulation ($n=50$). ARVC indicates arrhythmogenic right ventricular cardiomyopathy; D, desmosome; hiPSC, human induced pluripotent stem cell; hiPSC-CM, hiPSC-derived cardiomyocytes; G, glycogen; L, lipid droplets; M, mitochondria; Nuc, nucleus; and S, sarcomere.

troponin I (Figure IIIA in the online-only Data Supplement). Consistent with our finding in the first patient, real-time PCR analysis demonstrated significant reduction in the gene expression levels of *PKP2* ($P<0.05$) in the ARVC-B hiPSC-CMs compared with healthy control cells while showing similar levels of expression of *JUP* and *DSP* (Figure IIIB in the online-only Data Supplement). Similarly, immunostaining analysis of the ARVC-B hiPSC-derived cardiac tissue revealed reduced levels of PKP2 (Figure IIIA in the online-only Data Supplement). This was coupled with a reduction in the immunosignals of plakoglobin and Cx43 compared with control cells (Figure IIID and IIIE in the online-only Data Supplement).

Finally, electron microscopy analysis identified marked desmosomal abnormalities also in ARVC-B hiPSC-CMs (Figure IVA and IVB in the online-only Data Supplement) and the accumulation of lipid droplets in several of the diseased cells (Figure IVA and IVC in the online-only Data Supplement). Note again in the example provided (Figure IVD in the online-only Data Supplement) that the cells containing the distorted desmosomes (characterized by increased desmosomal widths) were also characterized by accumulation of lipid droplet clusters, recapitulating the findings in the first ARVC (c.972InsT) patient.

Vulnerability to Apoptosis

Apoptosis has been proposed as 1 of the mechanisms mediating CM loss in ARVC in both in vitro¹⁸ and in vivo²⁶ studies.

To assess for the presence of apoptosis, we performed terminal deoxynucleotidyl transferase dUTP nick end labeling analysis of both ARVC and healthy control hiPSC-CMs after exposure to serum starvation, a well-known stimulator of apoptosis. The results of these studies revealed a significantly higher percentage of apoptotic cells in the ARVC-hiPSC-CMs ($3.8\pm 1\%$; $n=7$; $P<0.05$; Figure V in the online-only Data Supplement) compared with healthy control cells ($1.0\pm 0.6\%$).

Effect of Adipogenic Stimulus

CMs derived from ARVC animal models were suggested to display a tendency toward adipogenesis.¹⁸ To evaluate whether ARVC-hiPSC-CMs recapitulate such a propensity, we exposed healthy control and ARVC-hiPSC-CMs to a combination of 3-isobutyl-1-methylxanthine, dexamethasone, and insulin in conjunction with lipid supplementation (MDI-Lipo). Treated healthy control cells exhibited minimal or no lipid droplet accumulation with preserved desmosomal and sarcomeric structures (Figure 7A). In contrast, the treated ARVC-hiPSC-CMs displayed extensive lipid droplet accumulation throughout most of the cytoplasm. Interestingly, this lipid accumulation was associated with paucity of desmosomal structures (Figure 7B).

Finally, we also evaluated whether the accumulation of lipid droplets in the ARVC-CMs after the adipogenic medium challenge could be prevented. Because previous studies implied that reduced canonical Wnt pathway signaling may

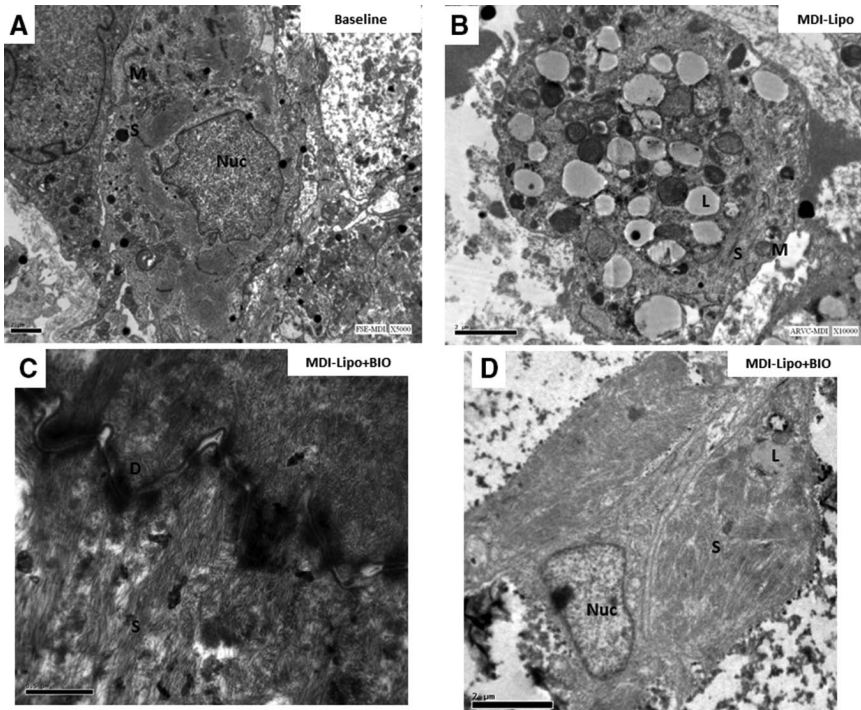


Figure 7. Effect of proadipogenic stimulus. **A** and **B**, Transmission electron microscopy images of healthy control (**A**) and arrhythmogenic right ventricular cardiomyopathy (ARVC; **B**) hiPSC-derived cardiomyocytes (hiPSC-CMs) exposed to lipogenic media. Note the absence of lipid droplets in control cells and the extensive lipid accumulation in the ARVC-hiPSC-CMs, compromising the majority of the cell's cytoplasm. The lipid clusters contained both low and high electron-dense lipid droplets (known to correlate with the presence of saturated and unsaturated fatty acids, respectively). **C** and **D**, Transmission electron microscopy images of the ARVC-hiPSC-CMs after simultaneous treatment with the lipogenic media and BIO. Note that BIO application did not reverse the desmosomal abnormalities in the ARVC-hiPSC-CMs (**C**) but significantly reduced lipid droplet accumulation in treated cells (**D**). D indicates desmosome; hiPSC, human induced pluripotent stem cell; L, lipid droplets; M, mitochondria; Nuc, nucleus; and S, sarcomere myofibrils.

be associated with the ARVC phenotype and lipid droplet accumulation,¹⁸ we aimed to determine the activity level of this pathway in the ARVC-hiPSC-CMs. To this end, we analyzed in both ARVC and control hiPSC-CMs the nuclear density of β -catenin; an immunostaining assay previously suggested to serve as a surrogate marker for canonical Wnt pathway activity.²⁷ Our results (Figure VI in the online-only Data Supplement) revealed a significant reduction in the nuclear density of β -catenin in the ARVC-hiPSC-CMs ($5.2 \pm 1.5\%$) compared with healthy control CMs ($12.1 \pm 1.8\%$; $P < 0.05$; $n = 7$), suggesting reduced Wnt activity in the former cells.

Next, to evaluate whether activation of the canonical Wnt pathway can reverse the lipid droplet accumulation, we treated the ARVC-hiPSC-CMs simultaneously with the adipogenic media with BIO (10 $\mu\text{mol/L}$), a specific inhibitor of GSK-3 β . This compound, a known activator of the canonical Wnt pathway, was previously shown to prevent lipid accumulation in vitro in cardiac progenitor cells derived from an ARVC mouse model.²⁸

Application of BIO did not affect sarcomeric organization in the ARVC-CMs and did not seem to significantly alter desmosomal abnormalities in these cells. Thus, quantitative ultrastructural analysis revealed that both desmosomal internal gap width (36 ± 2 versus 39 ± 5 nm) and external desmosomal width (169 ± 21 versus 214 ± 34 nm) did not significantly change after the addition of BIO to the adipogenic medium (Figure 7C). Similarly, a comparable low number of desmosomal structures were found in the ARVC-CMs treated with the adipogenic medium with or without simultaneous exposure to BIO (0.9 ± 0.2 versus 1.4 ± 0.6 desmosomes/cell). Importantly, in contrast to the lack of significant effects of BIO on the desmosomes, its application had a dramatic effect in preventing

intracellular lipid droplet buildup in the ARVC-hiPSC-CMs as can be appreciated in the example in Figure 7D.

Discussion

In the current study, we evaluated the ability of the hiPSC technology to model ARVC and provide mechanistic insights into the human disease process. Patient-specific hiPSCs were created from 2 patients with a clinical diagnosis of ARVC and genetic evidence for *PKP2* mutations.

By studying CMs differentiating from the ARVC-hiPSCs and comparing them with healthy control cells, we were able to (1) identify significant desmosomal abnormalities in the ARVC-hiPSC-CMs in both the electron microscopy studies and the *PKP2* and plakoglobin immunostaining analysis; (2) demonstrate the effect of desmosomal remodeling on the associated intercalated disc structure gap junction; (3) reveal the accumulation of lipid droplets in many of the ARVC-CMs and the upregulation of the proadipogenic transcription factor peroxisome proliferator-activated receptor- γ ; (4) identify a clear correlation between the degree of desmosomal abnormalities in the ARVC-CMs and the probability for lipid accumulation in the same cells; (5) show that ARVC-CMs have an increased vulnerability to apoptosis; and (6) demonstrate the ability of lipogenic stress to worsen the ARVC phenotype in terms of lipid droplet accumulation and the ability of the small molecule BIO (an inhibitor of GSK-3 β) to suppress the latter effect.

A major breakthrough in the understanding of ARVC came with the realization that this syndrome is associated with mutations in desmosomal proteins.^{3,4} Besides confirming the genetic nature of the disease (autosomal dominant inheritance with variable penetrance), this discovery fueled several studies attempting to uncover the relationship between such

mutations, the resulting desmosomal structural abnormalities, and the eventual ARVC pathological and clinical findings.^{3,18,29–31} Consistent with these findings, we also identified in the 2 patients studied (both presenting with a highly arrhythmogenic phenotype and advanced RV pathology) mutations in the *PKP2* gene. Both the novel mutation identified in our first patient (c.972InsT) and the previously reported mutation identified in the second patient (c.148_151delACAG/N) resulted in an early stop codon. As expected from the nature of such mutations (leading to a truncated protein), these allelic derangements resulted in a significant reduction in the density of the *PKP2* immunosignal in the ARVC-hiPSC-CMs. Interestingly, we could also identify a reduction in the mRNA levels of *PKP2* in the ARVC-hiPSC-CMs. This finding most probably results from a nonsense-mediated mRNA decay mechanism.³²

Importantly, in both patients, the *in vitro* ARVC-hiPSC-CM model was able to recapitulate the abnormal desmosomal phenotype, thought to be at the center of ARVC pathogenesis. This was manifested in the ultrastructural analysis of the ARVC-hiPSC-CMs by the presence of significant desmosomal abnormalities resembling those previously reported in patients with ARVC and murine models.^{3,30,33} Similarly, a significant reduction was noted in the density of the immunosignals of *PKP2* and the structurally associated desmosomal protein plakoglobin in the ARVC-hiPSC-CMs. The latter finding is in agreement with the work of Asimaki et al,³⁴ who observed a significant reduction in the immunosignal of both proteins in endomyocardial biopsies of patients with ARVC and with a recent study using a similar ARVC-hiPSC model.³⁵

In healthy myocardium, plakoglobin is found mainly at junctional plaques, and the cytoplasmic concentration of plakoglobin is kept low because of proteasomal degradation. In ARVC, the plakoglobin signal level at junctional plaques is diffusely reduced,^{34,36} and plakoglobin is thought to accumulate in the cytosolic pool, from which it can diffuse into the nucleus and alter gene expression.³⁷ The translocation of plakoglobin to the cytosolic and nuclear pools is thought to result in an attenuated spatial concentration at the desmosomes, translating to the reduced immunosignal identified in the current and previous studies^{34,36} at these membranous structures. In this regard, it is interesting to note that our real-time PCR data revealed an unaltered expression of plakoglobin at the mRNA level in both patients, despite the observed decrease in its membranous immunosignal levels, a finding that also supports the aforementioned hypothesis of desmosomal disintegration leading to cytoplasmic translocation of plakoglobin.

Recent studies suggest that abnormalities in the desmosomal proteins in ARVC may also affect other related components of the intercalated disc, including gap junctions and sodium channels.^{29,38} Supporting these previous observations, our results show a significant reduction in gap-junction density (as suggested from the Cx43 immunofluorescent analysis) in the ARVC-hiPSC-CMs compared with healthy control cells. To evaluate whether these structural findings translate into functional derangements, we quantified the field potential rise time in both ARVC and control CMs. Halbach et al,²⁴ using simultaneous microelectrode extracellular recordings and intracellular action potential measurements from embryonic CMs, previously demonstrated that the field potential

rise time highly correlates with action potential rise time and that reduced excitability and conduction can be identified by prolongation of this parameter. Consequentially, the presence of significantly prolonged field potential rise time in the ARVC-hiPSC-CMs suggests reduced excitability or conduction slowing in these cells and may contribute to the increased arrhythmogenesis observed in patients with ARVC, even before the development of significant ventricular structural alterations.

Another important finding of the current study relates to the identification of clusters of lipid droplets within many (approximately one third) of the ARVC-hiPSC-CMs. Consistent with this finding, we also observed a significant increase in the expression of the master proadipogenic transcription peroxisome proliferator-activated receptor- γ in the ARVC-CMs. Furthermore, we were able to demonstrate a functional proadipogenic state of the ARVC-CMs, as suggested by the robust lipid accumulation after exposure to a lipogenic media. The latter finding is in agreement with the recent article of Kim et al,³⁹ which also found that ARVC-hiPSC-CMs (derived from patients with ARVC with different *PKP2* mutations) are prone to lipid accumulation after treatment with various adipogenic stimuli.³⁹ Although lipid accumulation is considered one of the hallmarks of ARVC, there is uncertainty whether this is because of intramyocardial lipid accumulation or fibrofatty replacement of necrotic myocardial tissue. Intra-CM lipid accumulation was previously shown only in rodent models^{3,18,40} and in a few human myocardial specimens analyzed by electron microscopy.^{41,42}

Finally, the results of our study imply that a proadipogenic state of the diseased CMs resulting in intramyocardial lipid accumulation may have at least a partial role in ARVC disease pathogenesis. Interestingly, the effect of the adipogenic stimuli on the ARVC-CMs could be prevented by activation of the canonical Wnt pathway in these cells by the small molecule BIO, a specific inhibitor of GSK-3 β . This effect may be explained by the inherent reduced canonical Wnt pathway signaling in the ARVC-CMs as demonstrated by the reduced density of nuclear β -catenin in our study. In addition, these results are in agreement with the work of Lombardi et al,²⁸ who demonstrated that a similar treatment could prevent lipid accumulation in cardiac progenitor cells derived from a mouse model of ARVC.

One of the key novel findings of the current study was the fact that intracellular lipid droplet accumulation could be predicted based on the degree of desmosomal abnormalities in the same cell. The relationship among the mutations in desmosomal genes, desmosomal structural abnormalities, and the resulting fibrofatty myocardial phenotype in ARVC has been a long-standing enigma of the disease pathogenesis. A potential mechanism that may explain the tight relationship identified in our study between desmosomal abnormalities and lipid accumulation may be derived from recent findings by the Marian's group.^{18,28,43} These studies suggest a crosstalk between desmosomal disintegration and a proadipogenic state. Plakoglobin (γ -catenin) was pinpointed as a key mediator of this crosstalk, dislodging from the disintegrated abnormal desmosomes and inhibiting the canonical Wnt pathway because of its resemblance to β -catenin, consequentially promoting a proadipogenic state.¹⁸

Despite the unique advantages of the hiPSC approach for modeling inherited cardiac disorders in general and ARVC

specifically, as highlighted in this study, this strategy still possesses some inherent limitations such as the inability to study pathological phenomena at the whole-organ and systemic levels. This may be important, for example, for studying the potential mechanistic role of inflammation in ARVC.⁴⁴ Similarly, other factors that may play a role in ARVC pathogenesis, such as multicellular interactions, the 3-dimensional properties of the tissue, and external mechanical forces, cannot be modeled currently using the hiPSC-CM system. Further advancements in the field of in vitro cardiac tissue engineering, however, may provide a possible solution to these challenges.⁴⁵ An additional limitation stems from the relatively early stage phenotype of the hiPSC-CMs, which may not adequately represent the adult pathology. In this regard, it is interesting to note that recent studies suggested a potential role for early differentiating cardiac cells in ARVC pathogenesis.^{31,43} In addition, significant efforts are currently made in the field by several groups in an attempt to devise strategies to induce hiPSC-CM maturation.

Despite the aforementioned limitations, our data demonstrate the unique ability of the hiPSC technology to model ARVC. Using this approach, we showed that some of the key features of ARVC, namely, desmosomal-related pathology and lipid accumulation, can be identified in the ARVC-hiPSC-CMs. This study also provides important mechanistic insights into the cardiac pathology in ARVC as well as confirming some of the existing theories in patient-specific human tissues. Finally, the generated model system provides a unique platform to evaluate existing as well as novel therapeutic strategies for ARVC.

Acknowledgments

We thank Dr Doron Aronson for his statistical advice, Dr Edith Suss-Toby for her help in imaging, and Ira Minkov and Sharona Avital for their help in electron microscopy analysis.

Sources of Funding

This study was funded by the European Research Council Ideas program (ERC-2010-StG-260830-Cardio-iPS).

Disclosures

None.

References

- Basso C, Baucé B, Corrado D, Thiene G. Pathophysiology of arrhythmogenic cardiomyopathy. *Nat Rev Cardiol*. 2012;9:223–233.
- Saffitz JE, Asimaki A, Huang H. Arrhythmogenic right ventricular cardiomyopathy: new insights into mechanisms of disease. *Cardiovasc Pathol*. 2010;19:166–170.
- Yang Z, Bowles NE, Scherer SE, Taylor MD, Kearney DL, Ge S, et al. Desmosomal dysfunction due to mutations in desmoplakin causes arrhythmogenic right ventricular dysplasia/cardiomyopathy. *Circ Res*. 2006;99:646–655.
- Gerull B, Heuser A, Wichter T, Paul M, Basson CT, McDermott DA, et al. Mutations in the desmosomal protein plakophilin-2 are common in arrhythmogenic right ventricular cardiomyopathy. *Nat Genet*. 2004;36:1162–1164.
- Basso C, Corrado D, Marcus FI, Nava A, Thiene G. Arrhythmogenic right ventricular cardiomyopathy. *Lancet*. 2009;373:1289–1300.
- Lodder EM, Rizzo S. Mouse models in arrhythmogenic right ventricular cardiomyopathy. *Front Physiol*. 2012;3:221.
- Takahashi K, Yamanaka S. Induction of pluripotent stem cells from mouse embryonic and adult fibroblast cultures by defined factors. *Cell*. 2006;126:663–676.
- Takahashi K, Tanabe K, Ohnuki M, Narita M, Ichisaka T, Tomoda K, et al. Induction of pluripotent stem cells from adult human fibroblasts by defined factors. *Cell*. 2007;131:861–872.
- Zhang J, Wilson GF, Soerens AG, Koonce CH, Yu J, Palecek SP, et al. Functional cardiomyocytes derived from human induced pluripotent stem cells. *Circ Res*. 2009;104:e30–e41.
- Zwi L, Caspi O, Arbel G, Huber I, Gepstein A, Park IH, et al. Cardiomyocyte differentiation of human induced pluripotent stem cells. *Circulation*. 2009;120:1513–1523.
- Itzhaki I, Maizels L, Huber I, Zwi-Dantsis L, Caspi O, Winterstern A, et al. Modelling the long QT syndrome with induced pluripotent stem cells. *Nature*. 2011;471:225–229.
- Moretti A, Bellin M, Welling A, Jung CB, Lam JT, Bott-Flügel L, et al. Patient-specific induced pluripotent stem-cell models for long-QT syndrome. *N Engl J Med*. 2010;363:1397–1409.
- Lan F, Lee AS, Liang P, Sanchez-Freire V, Nguyen PK, Wang L, et al. Abnormal calcium handling properties underlie familial hypertrophic cardiomyopathy pathology in patient-specific induced pluripotent stem cells. *Cell Stem Cell*. 2013;12:101–113.
- Sun N, Yazawa M, Liu J, Han L, Sanchez-Freire V, Abilez OJ, et al. Patient-specific induced pluripotent stem cells as a model for familial dilated cardiomyopathy. *Sci Transl Med*. 2012;4:130ra47.
- Itzhaki I, Maizels L, Huber I, Gepstein A, Arbel G, Caspi O, et al. Modeling of catecholaminergic polymorphic ventricular tachycardia with patient-specific human-induced pluripotent stem cells. *J Am Coll Cardiol*. 2012;60:990–1000.
- Itzhaki I, Rapoport S, Huber I, Mizrahi I, Zwi-Dantsis L, Arbel G, et al. Calcium handling in human induced pluripotent stem cell derived cardiomyocytes. *PLoS One*. 2011;6:e18037.
- Zwi-Dantsis L, Huber I, Habib M, Winterstern A, Gepstein A, Arbel G, et al. Derivation and cardiomyocyte differentiation of induced pluripotent stem cells from heart failure patients. *Eur Heart J*. 2013;34:1575–1586.
- Garcia-Gras E, Lombardi R, Giocondo MJ, Willerson JT, Schneider MD, Khoury DS, et al. Suppression of canonical Wnt/beta-catenin signaling by nuclear plakoglobin recapitulates phenotype of arrhythmogenic right ventricular cardiomyopathy. *J Clin Invest*. 2006;116:2012–2021.
- Ross SE, Hemati N, Longo KA, Bennett CN, Lucas PC, Erickson RL, et al. Inhibition of adipogenesis by Wnt signaling. *Science*. 2000;289:950–953.
- Lindroos B, Boucher S, Chase L, Kuokkanen H, Huhtala H, Haataja R, et al. Serum-free, xeno-free culture media maintain the proliferation rate and multipotentiality of adipose stem cells *in vitro*. *Cytotherapy*. 2009;11:958–972.
- Taura D, Noguchi M, Sone M, Hosoda K, Mori E, Okada Y, et al. Adipogenic differentiation of human induced pluripotent stem cells: comparison with that of human embryonic stem cells. *FEBS Lett*. 2009;583:1029–1033.
- Marcus FI, McKenna WJ, Sherrill D, Basso C, Baucé B, Bluemke DA, et al. Diagnosis of arrhythmogenic right ventricular cardiomyopathy/dysplasia: proposed modification of the task force criteria. *Circulation*. 2010;121:1533–1541.
- Boulos M, Lashevsky I, Gepstein L. Usefulness of electroanatomical mapping to differentiate between right ventricular outflow tract tachycardia and arrhythmogenic right ventricular dysplasia. *Am J Cardiol*. 2005;95:935–940.
- Halbach M, Egert U, Hescheler J, Banach K. Estimation of action potential changes from field potential recordings in multicellular mouse cardiac myocyte cultures. *Cell Physiol Biochem*. 2003;13:271–284.
- den Haan AD, Tan BY, Zikusoka MN, Lladó LI, Jain R, Daly A, et al. Comprehensive desmosome mutation analysis in North Americans with arrhythmogenic right ventricular dysplasia/cardiomyopathy. *Circ Cardiovasc Genet*. 2009;2:428–435.
- Campian ME, Tan HL, van Moerkerken AF, Tukkie R, van Eck-Smit BL, Verberne HJ. Imaging of programmed cell death in arrhythmogenic right ventricle cardiomyopathy/dysplasia. *Eur J Nucl Med Mol Imaging*. 2011;38:1500–1506.
- Rabbani P, Takeo M, Chou W, Myung P, Bosenberg M, Chin L, et al. Coordinated activation of Wnt in epithelial and melanocyte stem cells initiates pigmented hair regeneration. *Cell*. 2011;145:941–955.
- Lombardi R, da Graca Cabreira-Hansen M, Bell A, Fromm RR, Willerson JT, Marian AJ. Nuclear plakoglobin is essential for differentiation of cardiac progenitor cells to adipocytes in arrhythmogenic right ventricular cardiomyopathy. *Circ Res*. 2011;109:1342–1353.
- Sato PY, Musa H, Coombs W, Guerrero-Serna G, Patiño GA, Taffet SM, et al. Loss of plakophilin-2 expression leads to decreased sodium current and slower conduction velocity in cultured cardiac myocytes. *Circ Res*. 2009;105:523–526.

30. Pilichou K, Nava A, Basso C, Beffagna G, Bauce B, Lorenzon A, et al. Mutations in desmoglein-2 gene are associated with arrhythmogenic right ventricular cardiomyopathy. *Circulation*. 2006;113:1171–1179.
31. Lombardi R, Marian AJ. Molecular genetics and pathogenesis of arrhythmogenic right ventricular cardiomyopathy: a disease of cardiac stem cells. *Pediatr Cardiol*. 2011;32:360–365.
32. Maquat LE. Nonsense-mediated mRNA decay in mammals. *J Cell Sci*. 2005;118(pt 9):1773–1776.
33. Rizzo S, Lodder EM, Verkerk AO, Wolswinkel R, Beekman L, Pilichou K, et al. Intercalated disc abnormalities, reduced Na(+) current density, and conduction slowing in desmoglein-2 mutant mice prior to cardiomyopathic changes. *Cardiovasc Res*. 2012;95:409–418.
34. Asimaki A, Tandri H, Huang H, Halushka MK, Gautam S, Basso C, et al. A new diagnostic test for arrhythmogenic right ventricular cardiomyopathy. *N Engl J Med*. 2009;360:1075–1084.
35. Ma D, Wei H, Lu J, Ho S, Zhang G, Sun X, et al. Generation of patient-specific induced pluripotent stem cell-derived cardiomyocytes as a cellular model of arrhythmogenic right ventricular cardiomyopathy. *Eur Heart J*. 2013;34:1122–1133.
36. Noorman M, Hakim S, Kessler E, Groeneweg JA, Cox MG, Asimaki A, et al. Remodeling of the cardiac sodium channel, connexin43, and plakoglobin at the intercalated disk in patients with arrhythmogenic cardiomyopathy. *Heart Rhythm*. 2013;10:412–419.
37. Saffitz JE. The pathobiology of arrhythmogenic cardiomyopathy. *Annu Rev Pathol*. 2011;6:299–321.
38. Joshi-Mukherjee R, Coombs W, Musa H, Oxford E, Taffet S, Delmar M. Characterization of the molecular phenotype of two arrhythmogenic right ventricular cardiomyopathy (ARVC)-related plakophilin-2 (PKP2) mutations. *Heart Rhythm*. 2008;5:1715–1723.
39. Kim C, Wong J, Wen J, Wang S, Wang C, Spiering S, et al. Studying arrhythmogenic right ventricular dysplasia with patient-specific iPSCs. *Nature*. 2013;494:105–110.
40. Matthes SA, Taffet S, Delmar M. Plakophilin-2 and the migration, differentiation and transformation of cells derived from the epicardium of neonatal rat hearts. *Cell Commun Adhes*. 2011;18:73–84.
41. Fujita S, Terasaki F, Otsuka K, Katashima T, Kanzaki Y, Kawamura K, et al. Markedly increased intracellular lipid droplets and disruption of intercellular junctions in biopsied myocardium from a patient with arrhythmogenic right ventricular cardiomyopathy. *Heart Vessels*. 2008;23:440–444.
42. Djouadi F, Lecarpentier Y, Hébert JL, Charron P, Bastin J, Coirault C. A potential link between peroxisome proliferator-activated receptor signaling and the pathogenesis of arrhythmogenic right ventricular cardiomyopathy. *Cardiovasc Res*. 2009;84:83–90.
43. Lombardi R, Dong J, Rodriguez G, Bell A, Leung TK, Schwartz RJ, et al. Genetic fate mapping identifies second heart field progenitor cells as a source of adipocytes in arrhythmogenic right ventricular cardiomyopathy. *Circ Res*. 2009;104:1076–1084.
44. Asimaki A, Tandri H, Duffy ER, Winterfield JR, Mackey-Bojack S, Picken MM, et al. Altered desmosomal proteins in granulomatous myocarditis and potential pathogenic links to arrhythmogenic right ventricular cardiomyopathy. *Circ Arrhythm Electrophysiol*. 2011;4:743–752.
45. Tiburcy M, Didié M, Boy O, Christalla P, Döker S, Naito H, et al. Terminal differentiation, advanced organotypic maturation, and modeling of hypertrophic growth in engineered heart tissue. *Circ Res*. 2011;109:1105–1114.

CLINICAL PERSPECTIVE

The study of inherited cardiac disorders has been hampered by the inability to derive patient-specific heart cells for in vitro analysis. The advent of the human induced pluripotent stem cell (hiPSC) technology has provided an exciting solution to this challenge. This technology allows to reprogram adult cells (such as fibroblasts) to yield pluripotent stem cell lines that could be coaxed to differentiate, in the culture dish, into human heart cells. Here, we describe the ability to use this emerging technology to model arrhythmogenic right ventricular cardiomyopathy (ARVC). ARVC is a primary heart muscle disorder resulting from desmosomal protein mutations characterized pathologically by fibrofatty infiltration and clinically by arrhythmias and sudden cardiac death. Dermal fibroblasts were obtained from 2 patients with ARVC (with plakophilin-2 gene mutations) and reprogrammed to generate hiPSCs. By studying the patient-specific hiPSC-derived cardiomyocytes (hiPSC-CMs), we were able to recapitulate the abnormal ARVC phenotype by identifying significant structural and functional abnormalities in the CM desmosomes and interestingly also in adjacent gap junctions. In addition, significant accumulation of lipid droplets was identified in several ARVC-hiPSC-CMs. Interestingly, the degree of desmosomal abnormalities correlated with the probability for lipid accumulation within the same cell. Finally, we demonstrate the ability of lipogenic stress to worsen lipid droplet accumulation in the ARVC CMs and of a small molecule inhibitor of GSK-3 β to prevent lipid accumulation in the same settings. These results highlight the unique potential of the hiPSC approach for mechanistic understanding of inherited cardiac disorders, studying basic biological phenomena, drug discovery, and personalized medicine.

SUPPLEMENTARY MATERIAL

Supplementary Methods

Genomic sequencing

Genomic DNA was isolated from the hiPSCs colonies using the high-pure PCR template preparation kit (Roche). The relevant DNA fragments of exon 3 of the plakophilin-2 (*PKP2*) gene were then amplified by PCR reaction using 100ng genomic DNA (primer sequences: forward TGACACATAACCACAGACAGTAC, reverse GTCAGTGAAAGTGCTTCTCTCA). The PCR products were then sequenced.

Teratoma formation and karyotype analysis

Undifferentiated hiPSCs were injected subcutaneously to immunodeficient SCID-beige mice. Teratomas, developing 8 weeks after injection, were harvested, cryosectioned (10 μ m) and stained with hematoxylin and eosin (H&E). Karyotype analysis was performed by the institution's cytogenetic laboratory according to standard procedures.

Immunostaining

For immunostaining, colonies of undifferentiated hiPSCs and enzymatically-dispersed hiPSCs-CMs were fixed with 4%-paraformaldehyde, permeabilized with 1%-Triton-X-100 (Sigma), blocked with 5%-horse serum and 1% bovine serum albumin. Specimens were then incubated overnight at 4°C with primary antibodies targeting: Tra-1-60, Oct-4, connexin-43(Cx43), plakoglobin (PKG) and beta-catenin (all from Santa Cruz), Desmin (Thermo scientific), Nanog (Abcam), α -fetoprotein(AFP) (Cell Marque), Nestin and cardiac troponin I (cTnI) (Chemicon), SSEA-4 (R&D), sarcomeric α -actinin (Sigma), plakophilin-2 (*PKP2*) (Acris, Germany) .

The preparations were incubated with secondary antibodies: donkey anti-mouse Alexa fluor[®]488-labeled immunoglobulin G (IgG) and Goat anti-mouse cy3-Immunoglobulin G

subclass2b (IgG2b) , donkey anti-rabbit Alexa fluor[®] 488-labeled IgG, donkey anti-goat Cy2-labeled IgG and donkey anti-mouse Alexa -labeled IgM (all from The Jackson Immunoresearch Laboratories, West Grove, Pa) at a dilution of 1:200 for 1hour. Nuclei were counterstained with DAPI (1:500, Sigma).The preparations were examined using a laser-scanning confocal microscope (Zeiss LSM-700). Alkaline-phosphatase staining of hiPSCs colonies was performed using Sigma detection kit.

The analysis of the immunofluorescence data were performed using images that were acquired using similar parameters and was conducted with the ImageJ software (NIH) and the image processing package Fiji¹ . Images were analyzed using pre-defined constant setting and a consistent automated densitometry algorithm. The density of the punctuate desmosomal (*PKP2*, Plakoglobin) and gap junction (Cx43) immunosignals was normalized to the total cardiomyocyte area (determined as the area positively stained for cTnI). For β -catenin nuclear density assessment, the ratio between nuclear β -catenin (co-localized with DAPI staining) and the total cellular β -Catenin signal in cTnI positive cells was calculated by the coloc2 analysis package in Fiji¹.

Gene expression analysis

RNA was isolated using the RNeasy-plus micro-kit (Qiagen). Reverse transcription into cDNA was conducted with the high-capacity cDNA reverse-transcription kit (Applied-Biosystems). Real-time PCR studies were conducted in triplicates using the Fast-SYBR Green-Master-mix and Taq-Man[®] Fast Universal PCR Master Mix (Applied –Biosytems) for SYBR-Green and Taq-Man detection, respectively. Primers are detailed in supplementary Table 1. Samples were cycled using the Fast ABI-7500 sequence detector. Conditions were: 20s at 95⁰C followed by 40 cycles of 3s-95⁰C and 30s-60⁰C. Cycle-threshold was calculated using default settings for the

real-time sequence detection software (Applied-Biosystems). Relative quantification was calculated according to the $\Delta\Delta\text{CT}$ method for quantitative real-time PCR (using an endogenous control gene).

Microelectrode array (MEA) recordings

To characterize the electrophysiological properties of the ARVC-hiPSCs-CMs, a multielectrode array (MEA) recording system (USB-MEA-256 system, Multichannel Systems, Reutlingen, Germany) was used. The contracting areas were micro-dissected and plated on fibronectin-coated MEA plates. The MEA system allows simultaneous recordings from 252 titanium nitride-coated gold electrodes (30 μm) at high spatial (100 μm) and temporal (15 kHz) resolutions. The local activation time at each electrode was determined as the timing of the maximal negative time derivative of the unipolar signal (dV/dt_{min}). The local activation times were then used to generate color-coded activation maps using custom-made MATLAB-based software. The recorded electrograms were also used to determine the local field potential (FP) duration (FPD). This parameter was previously shown to correlate with the action potential duration and to reflect the local QT interval. The estimated FPD was defined as the time interval between the initial deflection of the FP to return of the measured FP to baseline FPD measurements were normalized (corrected FPD [cFPD]) to the beating rate of the contracting areas with the Fredericia correction formula ($\text{cFPD} = \text{FPD} / [\text{RR}]^{1/3}$). To assess for the excitability and conduction velocity of the cells the field potential rise time of the cell was assessed. Field potential rise time was measured by blinded automated algorithm assessing the FPD rise time between 10% and 90% of voltage rise (ClampFit 10.3 software, Molecular devices, Sunnyvale, CA).

TUNEL staining

For TUNEL staining ARVC and control contracting areas were dissociated using 0.1% trypsin and plated on bovine fibronectin (1%) coated slides (all from Biological Industries, Israel). To induce apoptosis cells were exposed to serum free media for 20hours (DMEM F12, Life Technologies) prior to fixation. TUNEL staining was carried out according to manufacturer protocol (In Situ cell detection kit, TMR red, ROCHE) . Preparations were examined using a laser-scanning confocal microscope (Zeiss LSM-700). Analysis of the immunofluorescence data were performed using images that were acquired using similar parameters and was conducted with the ImageJ software (NIH).

Transmission electron microscopy

Spontaneously beating areas within the EBs (40 days of differentiation) were microdissected and fixed with cold 3.5%-glutaraldehyde in 0.1M sodium-cacodylate buffer. Specimens were post-fixed with 1% osmium-tetroxide and dehydrated using 50-100% ethyl-alcohol. For visualization, epon blocks were cut into thin-sections (70nm) and stained with 1% uranyl-acetate followed by 0.4% lead-citrate. Transmission electron microscopy was carried out using JEM 1011 (Jeol, Tokyo, Japan). Images were acquired and analyzed using Gatan digital micrograph software (Warrendale, PA). Quantitative morphological measurements were conducted by an experienced operator blinded to the studied specimens.

References:

1. Schindelin J, Arganda-Carreras I, Frise E, Kaynig V, Longair M, Pietzsch T, Preibisch S, Rueden C, Saalfeld S, Schmid B, Tinevez JY, White DJ, Hartenstein V, Eliceiri K, Tomancak P, Cardona A. Fiji: An open-source platform for biological-image analysis. *Nat Methods*. 2012;9:676-682

Legends for Supplementary Figures

Supplementary Figure 1: Clinical characteristics of the second ARVC patient.

[A] Electrocardiographic tracing showing the development of ventricular tachycardia in the second ARVC patient during programmed electrical stimulation. [B] Anteroposterior (AP) view of the electroanatomical unipolar voltage map of the RV of the second ARVC patient. Note the extensive area of low voltage (red indicates unipolar electrograms < 4mV), corresponding to the diseased regions in the RV inflow, outflow, and apex. [C] Sequencing of the plakophilin-2 (*PKP2*) gene in hiPSCs derived from the second ARVC patient (ARVC-B, right-panel) and of the healthy-control hiPSCs (left-panel). Note in the affected allele in the ARVC-B hiPSCs the presence of a deletion of ACAG in positions 148-151 in exon 1 (c.148_151delACAG/N).

Supplementary Figure 2: Characterization of the hiPSCs derived from the second ARVC patient (ARVC-B).

[A] Phase-contrast of the generated ARVC-B hiPSCs colonies demonstrating typical embryonic stem cell colony morphology. [B] Positive staining of the ARVC-B hiPSCs colonies for alkaline-phosphatase. [C] Immunofluorescent staining of the ARVC-B hiPSCs colonies for the pluripotency markers OCT4, NANOG, SSEA4, and TRA-1-60. [D] Immunostaining of *in-vitro* differentiating EBs for Desmin (mesoderm), alpha-Fetoprotein (AFP, endoderm) and Nestin (ectoderm). Scale-bars for A-D: 100µm. [E] Real-time quantitative PCR showing the down-regulation of *OCT3/4*, *KLF4* and *SOX2* transgenes in the ARVC-B-hiPSCs. Values are normalized to the house-keeping gene *RPL-7* and expressed as mean±SEM. Expression values (RQ(%)- Relative Quantitation (Percentage)) are relative to HEK293T cells (HEK) transiently transfected with the three plasmids to produce reprogramming virions. [F] Real-time quantitative

PCR evaluating the endogenous levels of the pluripotency genes *NANOG*, *FOXD3*, and *OCT 3/4* in healthy-control fibroblasts, ARVC-B fibroblasts and ARVC-B hiPSCs clones. Values are normalized to the house-keeping gene *RPL-7* and expressed as mean \pm SEM. Expression values (RQ) are relative to levels in the patient's fibroblasts.

Supplementary Figure 3: Desmosomal gene expression pattern and immunostainings

[A] Immunostaining of differentiating ARVC-B hiPSCs-CMs for the sarcomeric proteins cTnI (left) and α -actinin (right). [B] Real-time PCR analysis quantifying the expression of desmosomal proteins genes in the ARVC-B hiPSCs-CMs. Note the significant reduction in the expression of *PKP2* when compared to healthy-control cells (* p <0.05). No significant differences were noted in the expression levels of *JUP* (Plakoglobin) and *DSP* (Desmoplakin). Values are normalized to the house-keeping gene *RPL-7* and expressed as mean \pm SEM. Expression values (RQ (%)) are relative to control hiPSC-CMs. [C-E] Immunostainings of the ARVC-B hiPSCs-CMs for the desmosomal and gap-junction proteins. Note the reduced immunosignal levels of PKP2 (C), Plakoglobin (D) and Cx43 (E) in the ARVC-B hiPSCs-CMs (right-panel) when compared to healthy-control hiPSC-CMs (left-panel). Scale-bars for A,C-E: 25 μ m.

Supplementary Figure 4: Ultrastructural characterization of the ARVC-B hiPSCs-CMs.

Transmission electron microscopy image of the ARVC-B hiPSCs-CMs. [A-B] High-magnification images of distorted desmosomes (D) in ARVC-B hiPSCs-CMs. Note the presence of a structurally abnormal desmosome with a hazy configuration and a widened internal and

external desmosomal gap-widths. [C] Low-magnification image of the ARVC-B hiPSCs-CMs demonstrating the presence of lipid-droplet (L) clusters within the studied cardiomyocytes.

[D] Low-magnification image of the ARVC-B hiPSCs-CMs showing distorted desmosomes and accumulation of intracellular lipid-droplet clusters in the same cell. Abbreviations: S-sarcomere, Nuc-nucleus, M-mitochondria, L-lipid droplets, D-desmosome.

Supplementary Figure 5: Apoptosis in ARVC and healthy-control hiPSCs-CMs

The rate of apoptotic cells was evaluated in cells dissociated from contracting areas of healthy-control and ARVC-hiPSCs. To induce apoptosis, cells were exposed to serum starvation for 20 hours. Quantitative analysis revealed a significantly higher proportion of TUNEL positive nuclei in ARVC cells ($3.8\pm 1\%$) when compared to control cells ($1.0\pm 0.6\%$, $p=0.04$).

Supplementary Figure 6: β -catenin nuclear density in ARVC and control cardiomyocytes

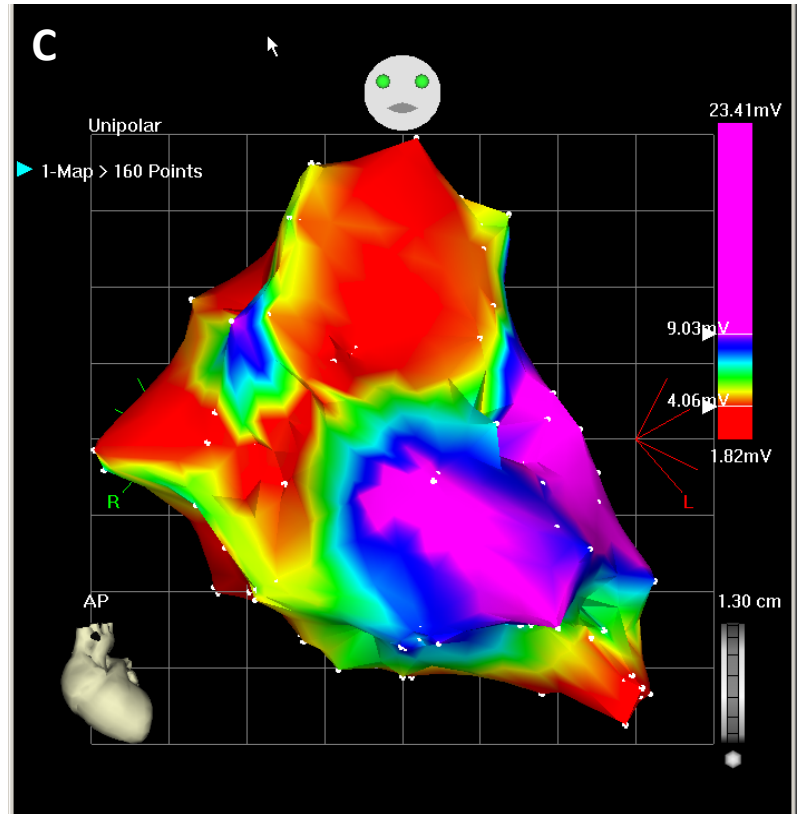
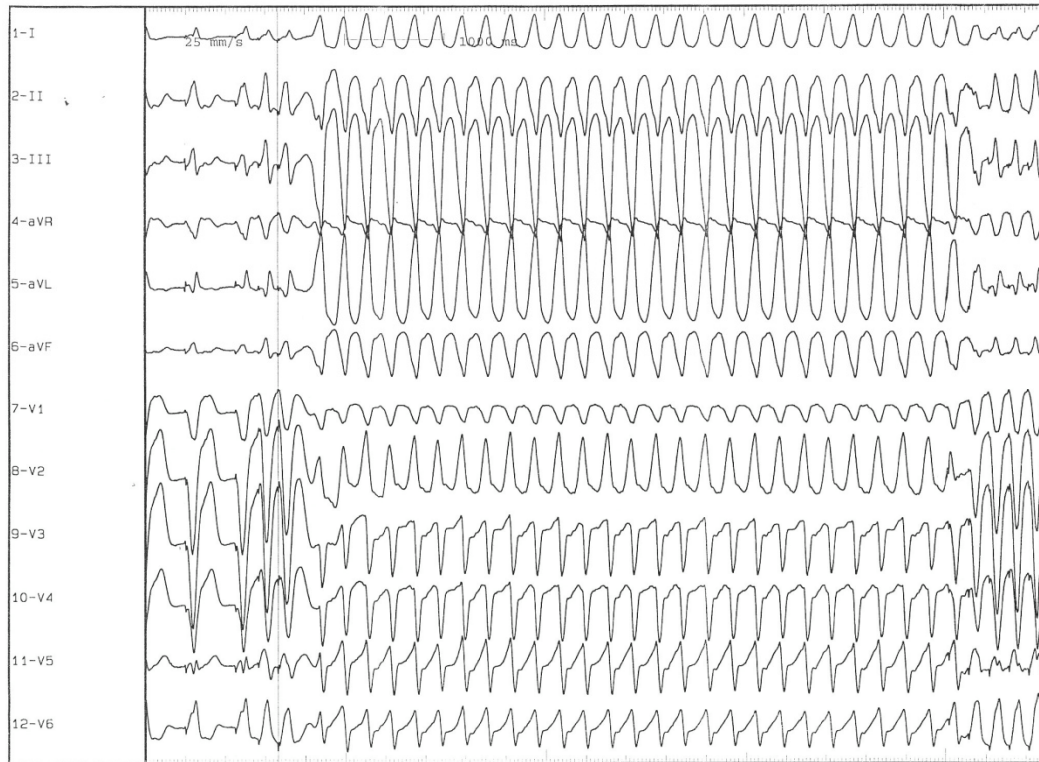
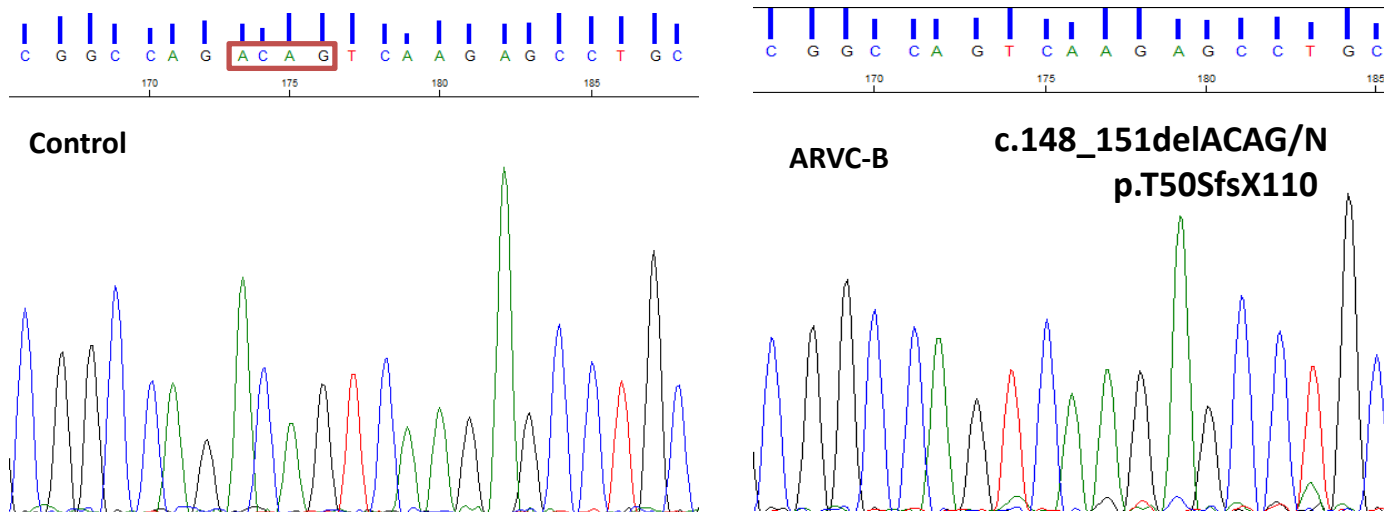
[A] Immunofluorescence staining for β -catenin in healthy-control (upper-panel) and ARVC (lower-panel) cardiomyocytes. The left-panel demonstrates the superposition of the nuclear staining (DAPI, blue), β -catenin staining (green) and the sarcomeric- α -actinin staining (red). Note the presence of nuclear β -catenin immunosignal in the healthy-control cells (arrows) but not in the ARVC cells. (Bar= $50\mu\text{m}$). (B) Quantitative assessment of the nuclear β -catenin density (a surrogate marker for canonical Wnt pathway activation). Note that the ARVC-hiPSCs-CMs displayed significantly reduced β -catenin density ($5.2\pm 1.5\%$) when compared to healthy-control cells ($12.1\pm 1.8\%$, $p=0.02$, $n=7$).

Supplementary Movie 1: Beating ARVC-derived hiPSC-CMs.

Supplementary Movie 2: Action-potential propagation within ARVC-hiPSCs-CMs as recorded by the multielectrode array (MEA) mapping system.

Supplementary Table 1 – Primers and probes for real-time PCR experiments

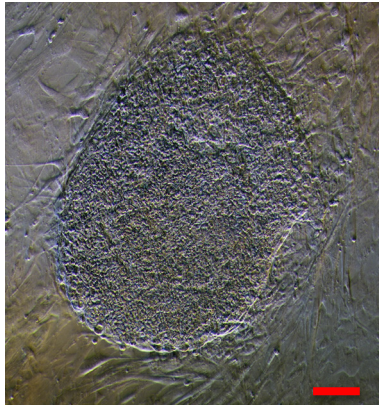
Gene	Sense	Anti-Sense	Probe (Taq-Man Real time PCR experiments)
Oct-3/4 Transgene	AGCCCTCACTTCACTGCACTGT	TTATCGTCGACCACTGTGCTGG	
Sox-2 Transgene	CCCAGTGTGGTGGTACGG	GCCCCCGAAGTTTGCT	
KLF4 Transgene	CTGCGGCAAAACCTACACAAA	TTATCGTCGACCACTGTGCTGG	
<i>Oct-3/4</i>	GAAAACCTGGAGTTTGTGCCA	TCACCTTCCCTCCAACCAGTT	
<i>FOXD3</i>	AAGCCCAAGAACAGCCTAGTG	GGGTCCAGGGTCCAGTAGTTG	
<i>NANOG</i>	TGCAAGAACTCTCAACATCCT	ATTGCTATTCTTCGGCCAGTT	
<i>MYL2</i>	CCTTGGGCGAGTGAACGT	GGGTCCGCTCCCTTAAGTTT	
<i>MYH7</i>	GGCAAGACAGTGACCGTGAAG	CGTAGCGATCCTTGAGGTTGTA	
<i>MYH6</i>	TCTCCGACAACGCCTATCAGTAC	GTCACCTATGGCTGCAATGCT	
<i>TNNI3</i>	CCAACTACCGCGCTTATGC	CTCGCTCCAGCTCTTGCTTT	
<i>ISL1</i>	GAGGGTTTCTCCGGATTTGG	TCCCATCCCTAACAAAGCATGT	
<i>RPL7</i>	GGCGAGGATGGCAAGAAA	CCTTTGGGCTCACTCCATTG	
<i>DSP</i>	CAGGATGTACTATTCTCGGCG	ATCAAGCAGTCGGAGCAGTT	
<i>GATA4</i>	TAGACCGTGGGTTTTGCATTG	CATCCAGGTACATGGCAAACAG	
<i>MLC2α (MYL7)</i>	CAGGCCCAACGTGGTTCTT	CCATCACGATTCTGGTCGATAC	
<i>MIXL1</i>	CGTGCCAAGTCTCGGCGTCA	ATGCCCCCTCCAACCCCGTT	
<i>MEF2C</i>	TAACTTCTTTTCACTGTTGTGCTCCTT	GCCGCTTTTGGCAAATGTT	
<i>PKP2</i>	GGTAGGAGAGGTTATGAAGAATGC	AAGCGATGAGAAGATGTGACG	CCAGATGACAAGGCCACGGAGAAAT
<i>JUP</i>	ACTGTAGTTACGCATGATCTGC	CTCAACAAGAACAACCCCAAG	TACGGCAACCAGGAGAGCAAGC
<i>PPARG</i>	GCTTATTGTAGAGCTGAGTCTTCT	CCATTACAAGAACAGATCCAG	AAAGTGCAATCAAAGTGGAGCCTGC
<i>RPL7</i>	AAGATTTGACGAAGGCGAAGA	GCAACTTCTATGTACCTGCAGA	AATGGAGTGAGCCCAAAGGTTCGA

A**B**

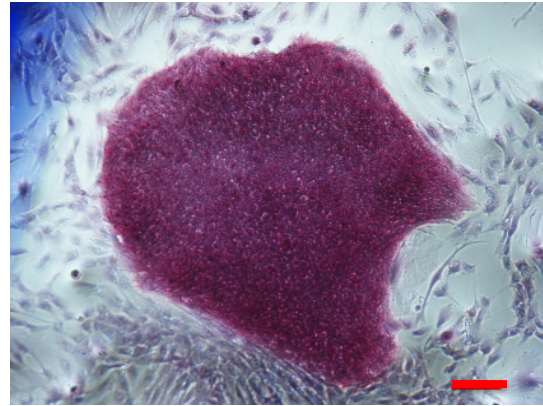
Supp. Figure 1

Supp. Figure 2

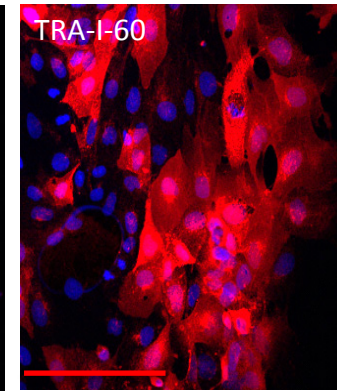
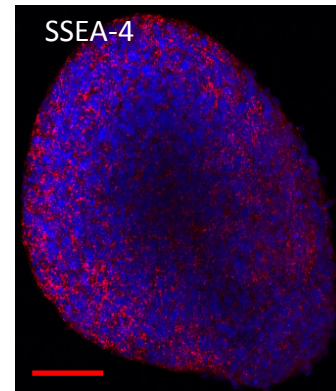
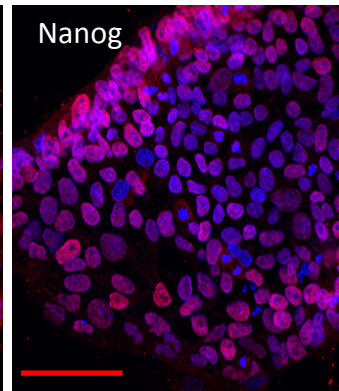
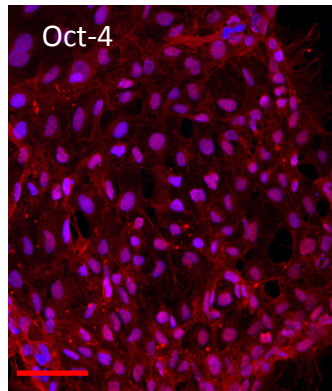
A



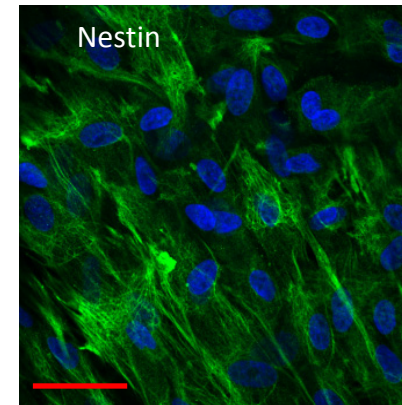
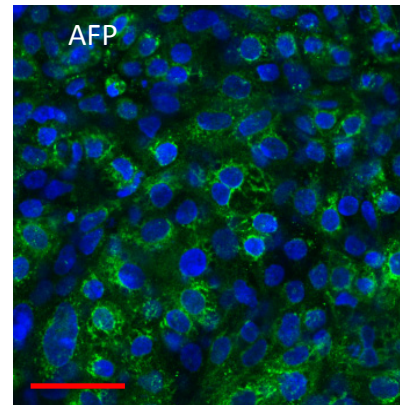
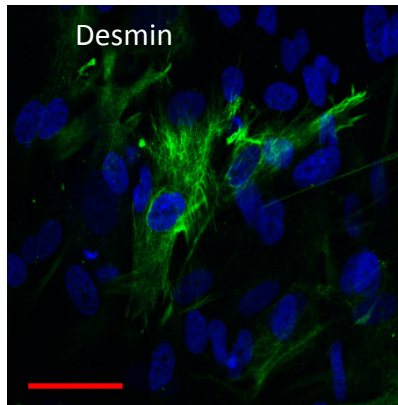
B



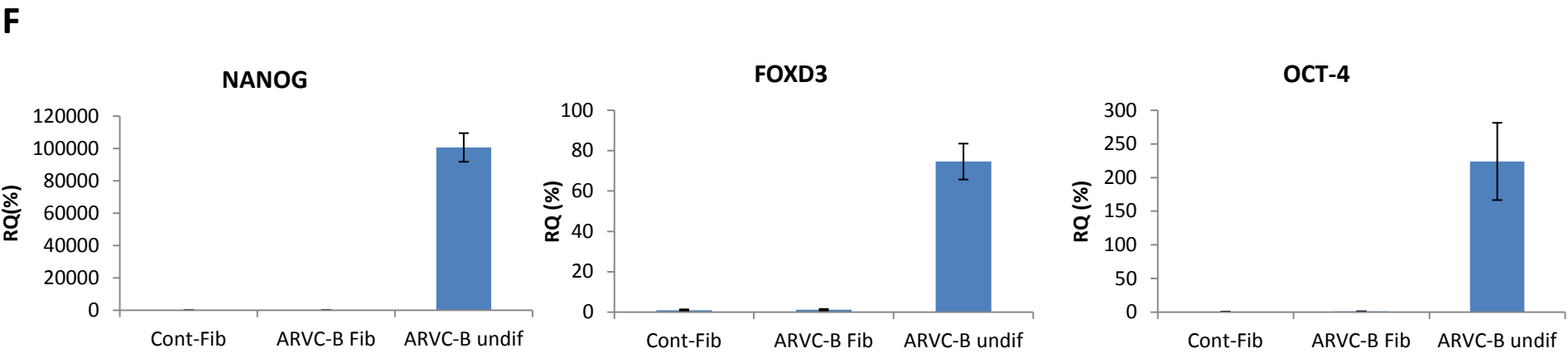
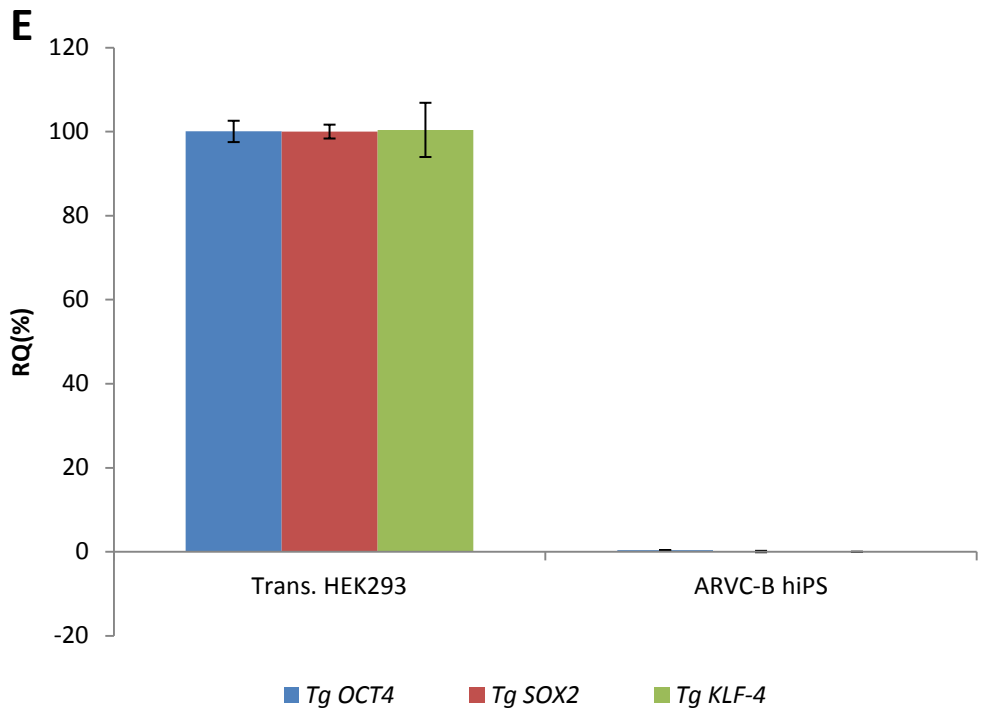
C



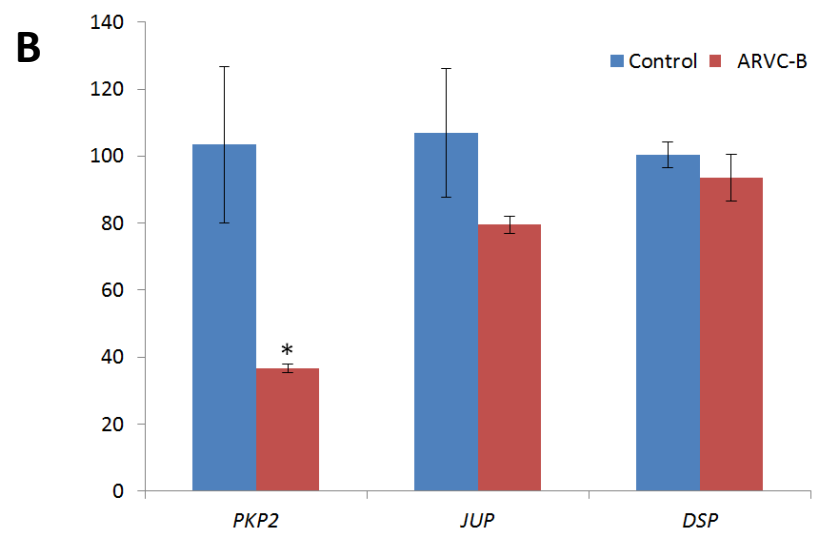
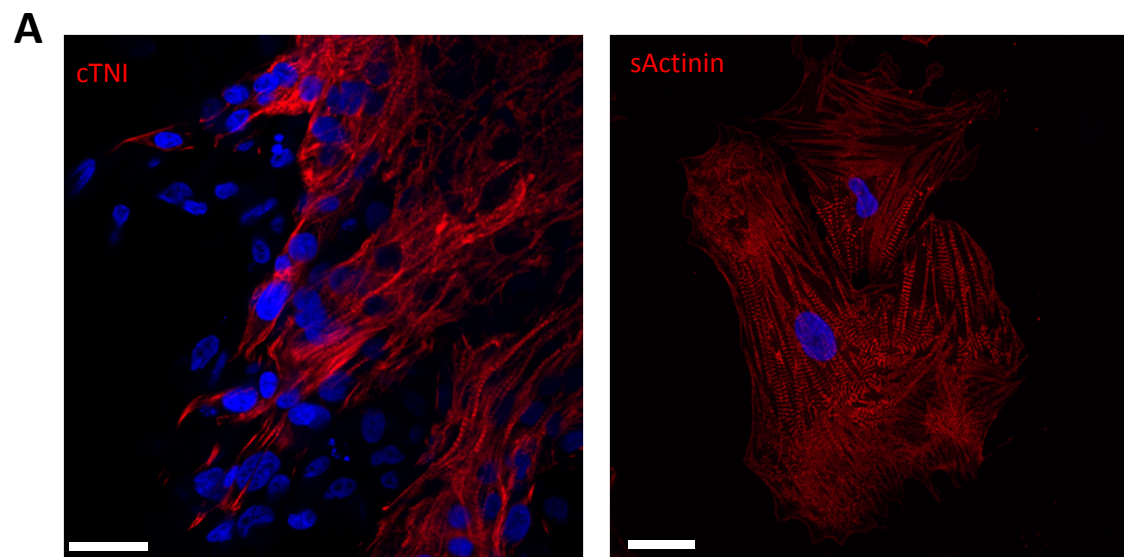
D



Supp. Figure 2 - continue



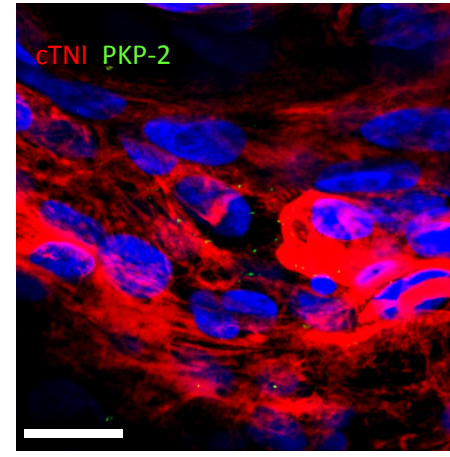
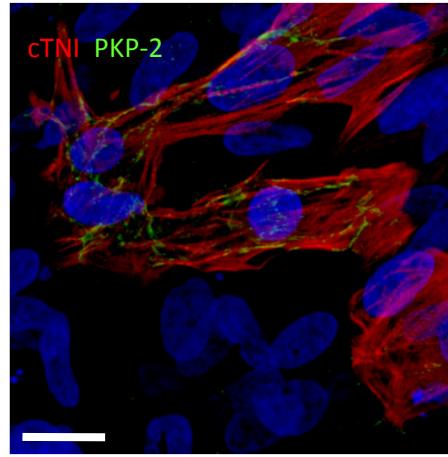
Supp. Figure 3



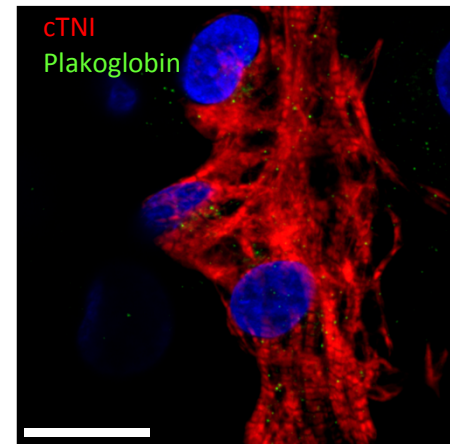
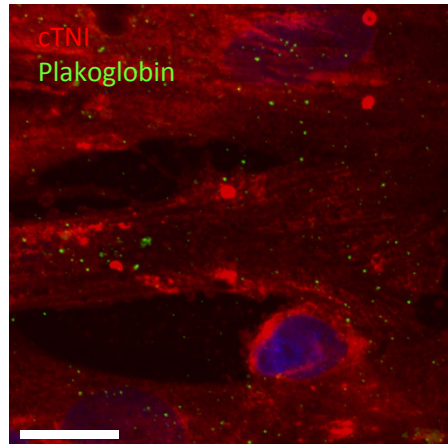
Control

ARVC-B

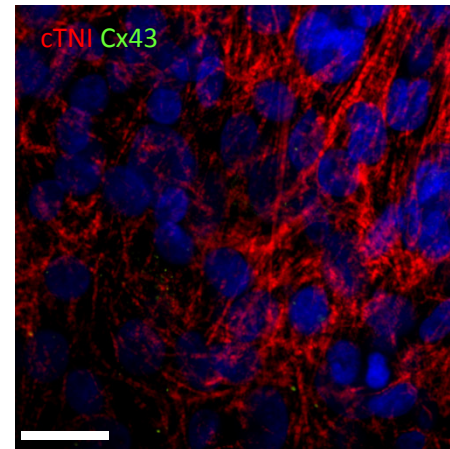
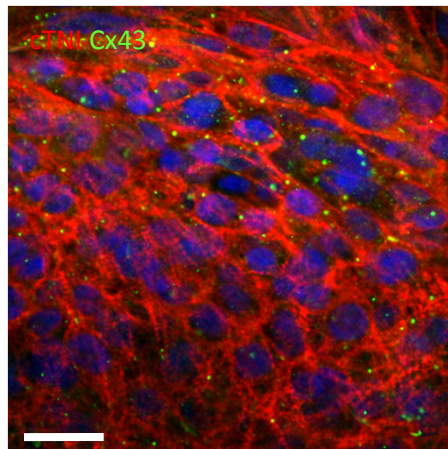
C



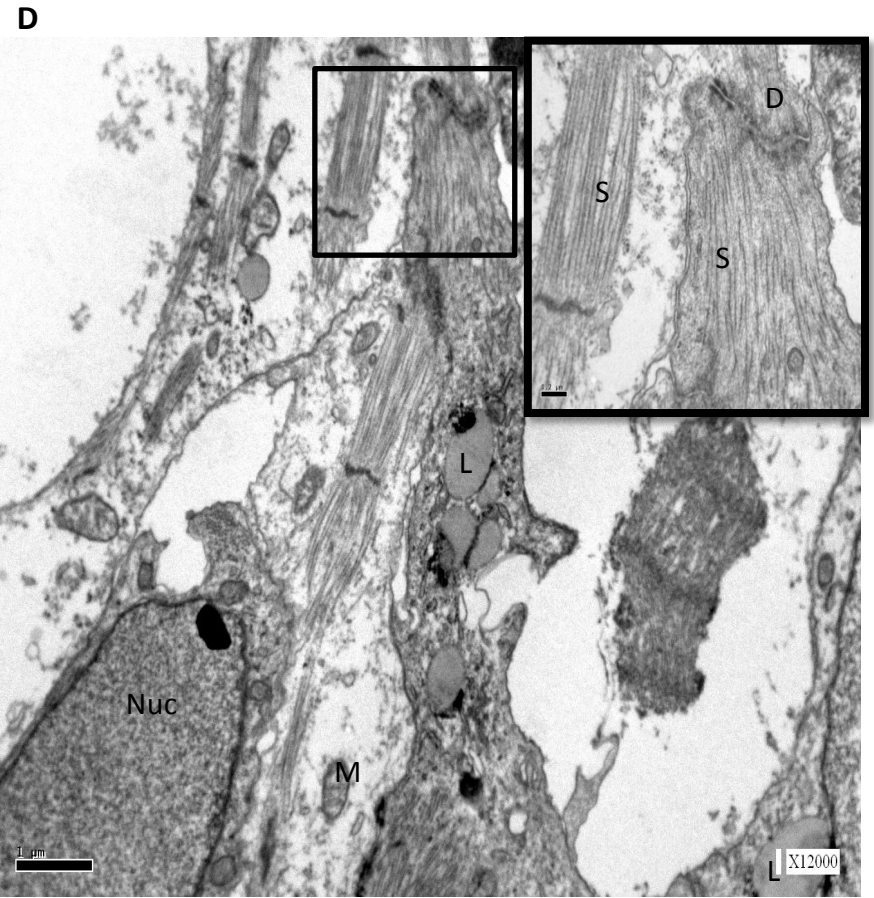
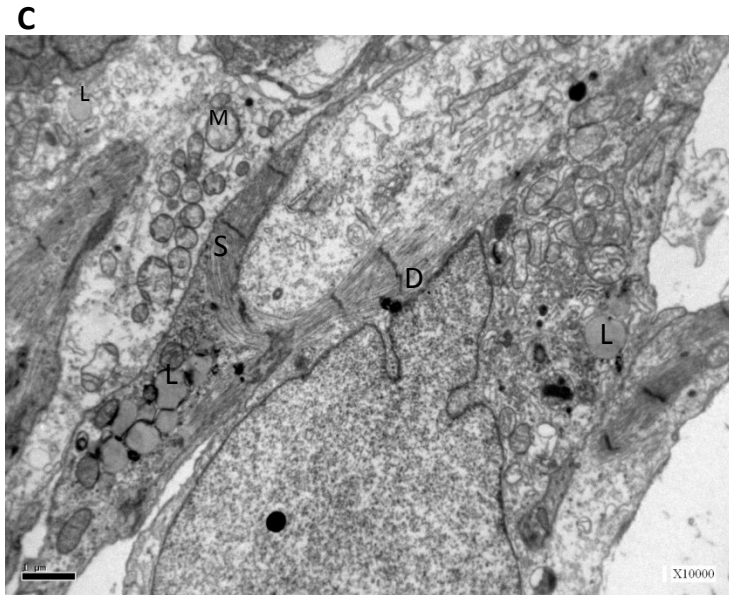
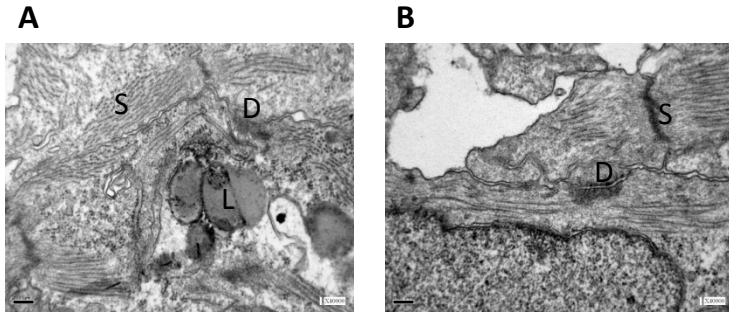
D



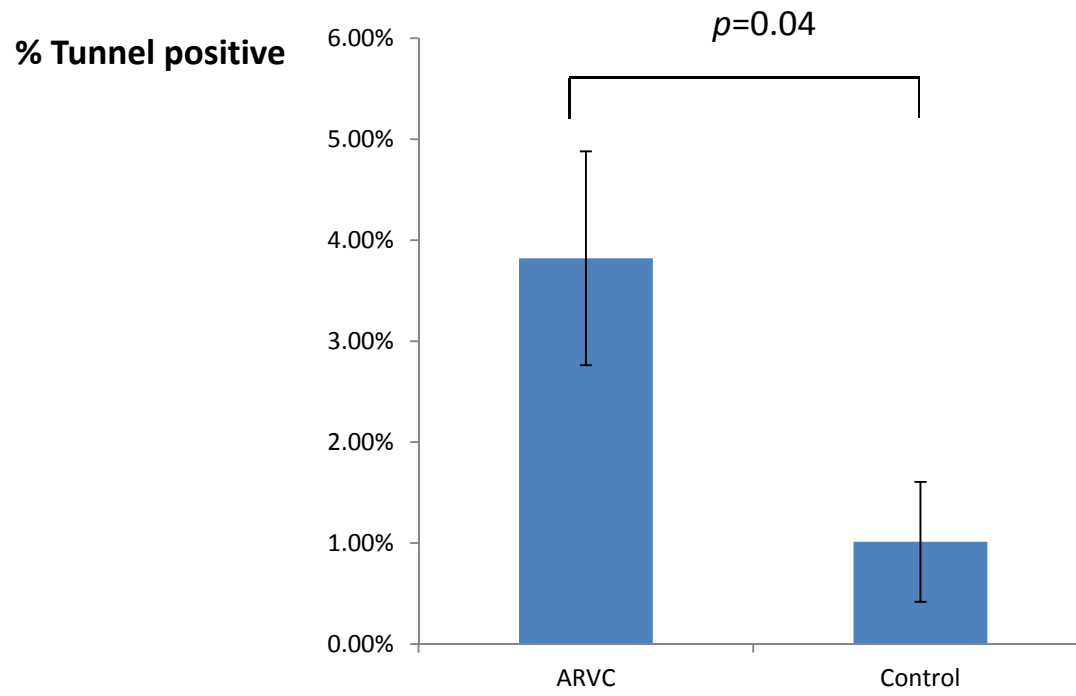
E



Supp. Figure 4

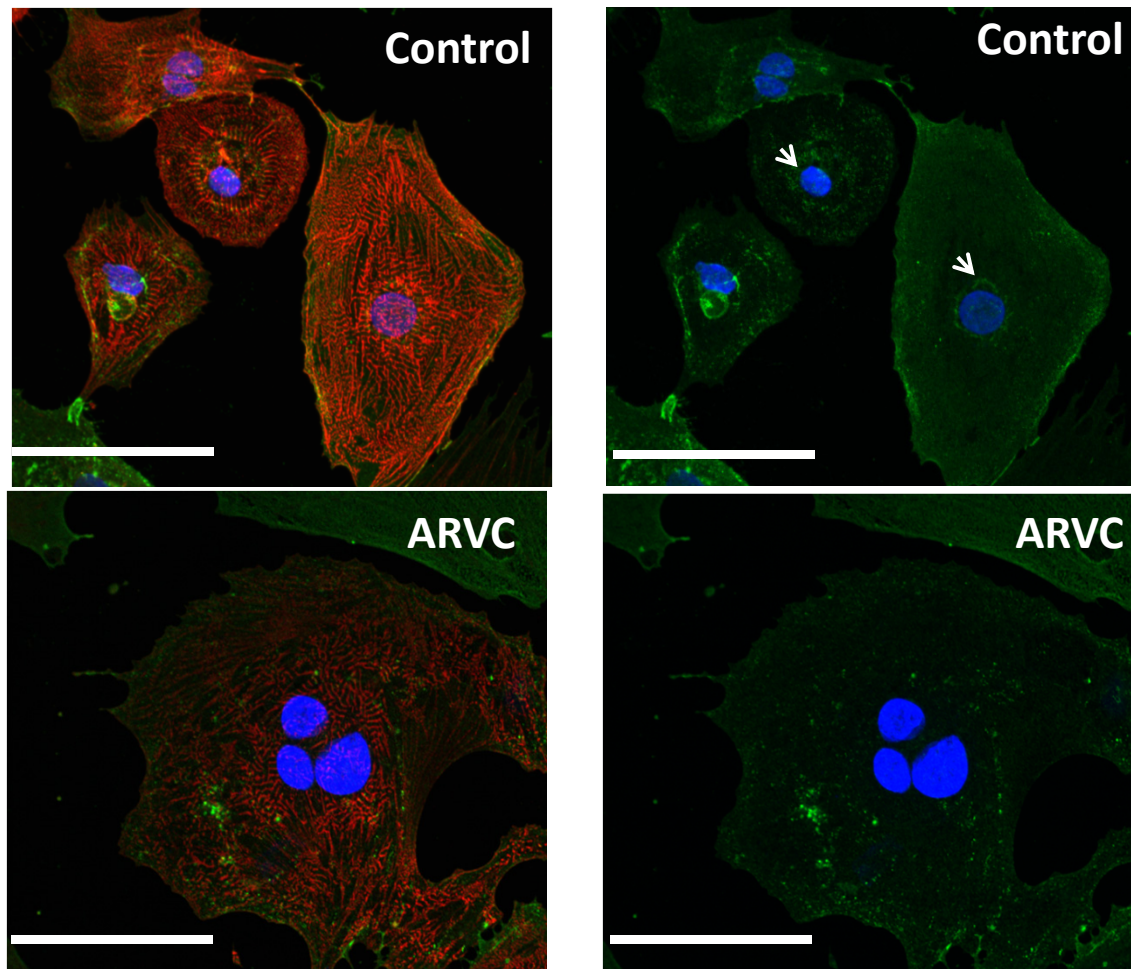


Supp. Figure 5



Supp. Figure 6

A



B

